



Canadian Geotechnical Journal

A coupled CFD-DEM investigation of internal erosion considering suspension flow

Journal:	<i>Canadian Geotechnical Journal</i>
Manuscript ID	cgj-2020-0099.R2
Manuscript Type:	Article
Date Submitted by the Author:	21-Aug-2020
Complete List of Authors:	Liu, Yajing; Zhejiang University Yin, Zhen-Yu; Hong Kong Polytechnic University, Department of Civil and Environmental Engineering Wang, Li-Zhong; Zhejiang University, Hong, Yi; Zhejiang University, College of Civil Engineering and Architecture
Keyword:	gap-graded soil, erosion, clogging, suspension, fine fraction
Is the invited manuscript for consideration in a Special Issue? :	Not applicable (regular submission)

SCHOLARONE™
Manuscripts

**A coupled CFD-DEM investigation of internal erosion considering
suspension flow**

Author 1

Yajing LIU, PhD candidate

Key Laboratory of Offshore Geotechnics and Material of Zhejiang Province, College of Civil
Engineering and Architecture, Zhejiang University, China

Email: yajing_liu@zju.edu.cn

Author 2

Zhen-Yu YIN*, Associate Professor

Department of Civil and Environmental Engineering, The Hong Kong Polytechnic
University, Hung Hom, Kowloon, Hong Kong, China

Email: zhenyu.yin@polyu.edu.hk; zhenyu.yin@gmail.com

Author 3

Lizhong WANG, Professor

Key Laboratory of Offshore Geotechnics and Material of Zhejiang Province, College of Civil
Engineering and Architecture, Zhejiang University, China

Email: wanglz@zju.edu.cn

Author 4

Yi HONG, Associate Professor

Key Laboratory of Offshore Geotechnics and Material of Zhejiang Province, College of Civil
Engineering and Architecture, Zhejiang University, China

Email: yi_hong@zju.edu.cn

***Corresponding author:**

Zhen-Yu YIN, Tel: +852 3400 8470; Fax: +852 2334 6389; Email:
zhenyu.yin@polyu.edu.hk; zhenyu.yin@gmail.com

A coupled CFD-DEM investigation of internal erosion considering suspension flow

Abstract: The influence of two-phase flows containing suspension particles, which are common in nature, on internal erosion with coupling effect of clogging remains unclear. This paper presents a three-dimensional coupled discrete element method and computational fluid dynamics (CFD-DEM) analysis of internal erosion considering different concentrations of suspension C (i.e., mass of the suspended particles in unit volume of fluid) in gap-graded granular soils with different fine fraction F_c (i.e., the percentage by mass of the fine particles in the gap-graded sample). The influences of C and F_c on the erosion and clogging behavior of soils are investigated from both the macroscopic and microscopic perspectives. It is found that for gap-graded samples being under-filled with $F_c=15\%$, the suspension flow (i.e., influent fluid with suspending particles) decreases the cumulative eroded fine particle loss and the increasing rate of soil hydraulic conductivity due to clogging at the top of the sample. The degree of clogging is found to jointly be determined by both constriction size distribution and the suspension concentration. Clogging in a local area usually occurs with the formation of the clusters which has a high resistance to the drag force applied by the fluid flow.

Keywords: gap-graded soil, erosion, clogging, suspension, fine fraction, constriction size

50 **1. Introduction**

51 Internal erosion may occur when the coarse grain group of a gap-graded sandy soil is
52 unable to prevent the erosion of the fine particles under the action of seepage. This issue has
53 been studied extensively by various researchers (Skempton and Brogan 1994; Indraratna et al.
54 2007; Chang and Zhang 2013; Shire et al. 2014; Santos et al. 2015; Benamar et al. 2019; Yang
55 et al. 2019, 2020). The geometrical condition, hydraulic loading and in-situ stress conditions,
56 i.e., the gap ratio (i.e., the ratio of the minimum particle diameter in the coarse grain group to
57 the maximum particle diameter in the fine grain group), fine fraction (F_c), hydraulic gradient
58 (i) and mean effective stress (p') are identified as the most influential factors that govern the
59 initiation and evolution of internal erosion.

60 Previous studies on internal erosion usually assumed that the inflow applied to the sample
61 is pure fluid without any suspension particles. In reality, the seepage flow through soils usually
62 contains dispersed suspension particles with the size ranging from fractions of a millimeter
63 down to macromolecular dimensions (Amir and Brij 2009). The presence of the suspension
64 particles within the inflow is may eventually cause to cause clogging in the gap-graded soil,
65 with consequences to change the soil structure, the hydraulic properties and mechanical
66 behavior of the soil. The seepage flow containing suspension particles could either destabilize
67 the primary load-bearing structure to weaken the soil strength by inducing dislodgement of soil
68 grains (Hicher 2013; Yin et al. 2014, 2016;), or strengthen the primary fabric to increase the
69 soil strength by introducing more load-bearing fine particles into the gap-graded soil. As far as
70 the hydraulic property is concerned, the seepage flow containing suspension particles is likely
71 to reduce the void ratio and soil hydraulic conductivity (Alem et al. 2015; Sato and Kuwano

72 2015; Yang et al. 2020), by single-particle plugging or by particulate bridging at pore throats
73 (Valdes and Liang 2006). Limited experimental data have shown that the soil hydraulic
74 conductivity could be reduced by more than 50% by seepage flow containing a low
75 concentration (e.g., 0.5 g/L) of suspension particles (Reddi et al. 2005). Thus, the seepage flow
76 containing suspension particles could have significantly affected the hydro-mechanical
77 behavior of granular soils during internal erosion.

78 Although many significant macroscopic phenomena have been obtained from the existing
79 experimental investigations, a limited number of numerical studies have been performed to
80 understand the underlying microscopic mechanisms for the experimental observations. As a
81 result, some important microscopic insights of internal erosion and clogging, e.g., the
82 transportation or distribution of suspension particles within gap-graded samples has yet not
83 been well understood. Due to the complex interactions between the fluid and soil particles
84 during the coupled processes of erosion and clogging, the numerical methods which only
85 capture single-phase behavior (either for the solid or liquid phase) are insufficient for the
86 purpose. A combination of computational fluid dynamics (CFD) and the discrete element
87 method (DEM) has been emerging as a powerful tool for modeling the particle-fluid system in
88 recent studies (Zhao and Shan 2013; Zhao et al. 2016; Kawano et al. 2018; Hu et al. 2019).

89 This paper aims to study the influence of seepage flows containing suspension particles
90 on the clogging, erodibility and hydro-mechanical behavior of granular soils from both macro-
91 and microscopic perspectives, through a 3D coupled CFD-DEM investigation. Key influence
92 factors considered in the numerical analyses include suspension concentrations in the seepage
93 flow (C), fine fraction in the gap-graded soil (F_c) and hydraulic gradient (i). Macroscopic

94 observations in various aspects, including cumulative eroded particle mass, sample
95 deformation, hydraulic conductivity, erosion rate and stress-strain relations, are presented with
96 their responses to different C and F_c . The microscopic mechanisms underpinning these
97 macroscopic observations are also analyzed, in the context of transportation and clogging of
98 suspension particles within gap-graded samples, the evolution of load-bearing structure and
99 constriction size distributions.

100 **2. Coupled CFD-DEM method**

101 The coupled CFD-DEM method used in this study includes formulations for three key
102 elements, i.e., the discrete element method (DEM), computational fluid dynamics (CFD) and
103 the coupling between CFD and DEM. In this study, the open-source DEM code LIGGGHTS
104 3.7.0 (Kloss et al. 2012) and CFD code OpenFOAM 5.0 (Jasak et al. 2007) are adopted for
105 simulating massive dispersed particle bodies and hydrodynamic processes, respectively. The
106 particle-fluid interaction forces, including the drag force, pressure gradient force and viscous
107 force, are computed by coupling the CFD and DEM codes (Goniva et al. 2012; Kloss et al.
108 2012). Governing equations for DEM, CFD, and coupling between CFD and DEM have been
109 given elsewhere (Hu et al. 2019), and are summarized in the Appendix.

110 The coupled CFD-DEM method is validated according to Chang (2012), in which a series
111 of internal erosion tests were performed on real gap-graded granular soil under different
112 effective confining stresses (σ'_c) and hydraulic gradients (i). Considering the similarity between
113 Chang (2012) and this study in the stress and hydraulic conditions, the experimental results
114 reported in Chang (2012) are used here to validate the numerical CFD-DEM model. In some
115 cases of the experiment, the specimen was tested under isotropic stress states with mean

116 effective stress (p') of 50 and 200 kPa. The hydraulic gradient, i , was increased in stages from
117 0 to the final value (i.e., 0.15 per 10 minutes for $i < 1.0$, 0.25 per 10 minutes for $1.0 < i < 2.0$, and
118 0.50 per 10 minutes for $i > 2.0$). More details are introduced in Chang (2012).

119 Fig. 1 shows the grain size distribution of the gap-graded granular materials with $F_c=35\%$
120 used in the experiment and validation model. The gap-graded material with $F_c=15\%$ and 35%
121 in Fig. 1 is adopted in the analysis of internal erosion with suspension particles. The material
122 with a low gap ratio and a narrow range of grain diameter is used in the simulation to reduce
123 the total number of DEM particles and improve calculation efficiency. For the sake of
124 computational efficiency, the hydraulic gradient in simulations was increased by one level
125 every 2.0 s. Although the simulation duration is very short compared with that in the laboratory
126 test, the simulated results below show that it is sufficient to reproduce the experimental results
127 in trend. Table 2 summarizes the parameters used in the validation model.

128 Fig. 2(a) shows the simulated and experimental results for the cumulative eroded particles
129 mass during erosion. Both simulated and experimental results present that the specimen under
130 $p'=200$ kPa has a higher critical hydraulic gradient and a larger final cumulative eroded
131 particles mass compared with those of the specimen under $p'=50$ kPa. The tests showing
132 intensified erodibility of the samples by higher p' , e.g., the cumulative eroded particles mass
133 increasing with p' , are also reported by Bendahmane et al. (2008). Figs. 2(b) and 2(c) show the
134 vertical strain and transverse strain of the samples under $p'=50$ and 200 kPa. The simulated
135 results are in good agreement with the experimental results in trend, which demonstrates the
136 predictive capability of the CFD-DEM method for capturing the main characteristics of soil
137 behavior during internal erosion. The scatters between the measured and simulated results are

138 probably caused by some simplifications of the numerical model, e.g., the difference in
139 gradation between the experimental and numerical soils, spherical particles, short simulation
140 time, etc.

141 The critical i for the occurrence of internal erosion in the simulations is smaller than that
142 of the experiments. This is because all particles in the simulations are spherical, for which the
143 voids formed by coarse particles are larger than that formed by the real soil particles with non-
144 spherical shape, e.g., flat, ellipse or prism. The spherical fine particles are also more likely to
145 get through the voids formed by the coarse particles and hence eroded under the action of
146 seepage flow. The influences of particle shape on erosion will be analyzed in future work.

147 **3. Simulation program and model setup**

148 **3.1 Simulation program**

149 The simulation program includes 12 cases to study the effects of suspension concentration
150 (i.e. particle concentration in pore fluid according to Reddi et al. (2005) where particles are not
151 contacted each other), fine fraction in the gap-graded soil and hydraulic gradient on internal
152 erosion, as summarized in Table 1. Fig. 1 shows the particle size distributions of the two gap-
153 graded samples with $F_c=15\%$ and 35% for the current study. It is inferred from the previous
154 studies (Skempton and Brogan 1994; Minh et al. 2014; Shire et al. 2014) that, for samples with
155 $F_c=15\%$, the fine particles are likely to under-fill the voids between coarse particles and play a
156 diminished role in stress transfer. In contrast, when the fine fraction exceeds about 25% (e.g.,
157 35%), the fine particles are found to start overfilling the voids between coarse particles, to carry
158 loads for stabilizing the force transmission structures. Thus, the gradations used in this study
159 represent two typical fabrics of the gap-graded sandy soil. According to Burenkova method

160 (1993), the soil is internal unstable (i.e., internal erosion occurs when the hydraulic gradient
161 reaches the critical hydraulic gradient) if d_{90}/d_{60} of the soil satisfies the following equations:

$$0.76 \log(d_{90}/d_{15}) + 1 < d_{90}/d_{60} < 1.86 \log(d_{90}/d_{15}) + 1 \quad (1)$$

162 where d_{15} , d_{60} and d_{90} are the sizes of grain at which 15%, 60% and 90% of particles by weight
163 are smaller, respectively. Fig. 3 shows the assessment of internal stability for the samples with
164 $F_c=15\%$ and 35% by Burenkova method. It is shown that both samples are susceptible to
165 internal erosion. In this study, the suspension particles are assumed to come from the upstream
166 soil (Goldsztein 2005). The suspension particle size distribution in the influent is the same as
167 that of the fine fraction of the sample. This study focuses on the influence of the physical
168 clogging of suspension particles on the internal erosion of the gap-graded soil. The cohesion
169 of the suspension particles is not considered. Some previous studies (Zamani 2009; Zheng et
170 al. 2014) on pore-clogging by the suspension particles also did not take into account the
171 cohesion of suspension as an influential factor.

172 The previous experiments (Skempton and Brogan 1994; Li 2008) have shown that the i_c
173 is usually smaller than 0.3 for coarse-grained soils. Thus, the hydraulic gradient $i=0.10, 0.25$
174 was selected in this study, which broadly covers the typical ranges of the critical hydraulic
175 gradient for the initiation of internal erosion. Two relatively high suspension concentrations,
176 i.e., of 30 and 60 g/L, are selected in this study to facilitate clogging of suspension particles in
177 a short simulation time (15.0 s). During the entire simulation process, a constant isotropic
178 pressure (p') of 50 kPa is posed to each sample. Internal erosion where fine particles are washed
179 out the soil matrix can happen in different directions of flow. The current study focuses on the
180 downward migration of the fine particles, which usually occurs on the supported side of the

181 retaining wall. As the maximum pressure induced by the gravity force (lower than 1 kPa) is
182 significantly lower than the 50 kPa of confinement (Kawano et al. 2018), the gravity force is
183 not considered in this study to eliminate its influences on the particle detachment and migration
184 (Wautier et al. 2019; Hu et al. 2019). In this case, a lot of fine particles within the sample are
185 floated or only have one contact, which further decreases the critical i of the sample.

186 3.2 Model geometry and parameters

187 Fig. 4 shows a cuboid sample consisting of spherical particles, with a size of 13 mm×13
188 mm×26 mm ($14D_{50} \times 14D_{50} \times 28D_{50}$). D_{50} is the diameter at 50% mass passing. The CFD domain
189 overlaps the DEM domain with a size of 13.5 mm×13.5 mm×35 mm. An upstream region with
190 a size of 13 mm×13mm×5 mm was defined on the top of the cuboid sample to generate
191 dispersed suspension particles (SPs) in the influent. The CFD domain is larger than the DEM
192 one to ensure that all particles in the sample are immersed in the fluid and subjected to the
193 fluid-particle interaction forces. In the coupled CFD-DEM method, the boundary conditions
194 applied on CFD and DEM domains are in fact independent with each other. Each domain has
195 its independent boundary conditions to ensure a correct calculation for granular materials or
196 fluid flow. To maintain a constant particle concentration, the number of the suspension particles
197 in the upstream region was regulated for each 0.01 s during the entire simulation period (15.0
198 s). The parameters for the particle properties, i.e., elastic modulus (E), friction coefficient (μ_f)
199 and rolling friction coefficient (μ_r), are adopted according to previous DEM studies modeling
200 the mechanical behavior of sand (Wang and Gutierrez 2010; Yang et al. 2017). The rolling
201 friction impedes the rotation of particles, which certainly prevents the detachment and
202 migration of the fine particles to some degree. In this study, the value of rolling friction is 0.1

203 which is typically adopted in some previous numerical studies on granular materials (Goniva
204 et al. 2012; Yang et al. 2017). Some cases without rolling friction are also simulated to reveal
205 its influences on internal erosion preliminarily, which is shown in section 4.1. The time step in
206 CFD and DEM is adopted as 1×10^{-4} s and 5×10^{-7} s, respectively. The difference in the size of
207 time step in CFD and DEM is larger compared to other CFD-DEM coupling studies on internal
208 erosion (e.g. Hu et al. 2019; Nguyen and Indraratna 2020a). Nevertheless, Zhao and Shan (2013)
209 found that the numerical results of the coupled CFD-DEM method agree well with the
210 analytical solutions of one-dimensional consolidation when the time step in CFD and DEM
211 equals 5×10^{-4} s and 5×10^{-7} s, respectively. Table 2 summarizes the simulation settings.

212 3.3 Boundary conditions

213 In each numerical analysis, constant differential pressure between the inlet and outlet
214 boundaries of CFD domain was applied to maintain the hydraulic gradients ($i = \Delta p / \rho g L$, where
215 Δp is the differential pressure and L is the sample length in the flow direction) of $i = 0.10$ or
216 0.25 across the sample length. Free slip boundary conditions were applied on the four lateral
217 walls, meaning that the surface fluid was restricted to move along the wall.

218 For the boundary conditions of DEM, an isotropic stress of $p' = 50$ kPa was applied to each
219 DEM sample using a servo wall algorithm. The friction coefficient of the confining wall was 0
220 while its elastic stiffness was 10 times larger than that of the particle. The friction of the wall
221 is set as 0 to prevent the generation of shear stress at the boundary of the sample, which is also
222 adopted in some previous numerical research on interna erosion with the coupled CFD-DEM
223 method (Wautier et al. 2018; Wautier et al. 2019). If the wall is relatively smooth, previous
224 studies show that it is likely to facilitate the erosion of the fine particles near the wall and

225 decrease the critical hydraulic gradient (Moffat et al. 2011; Nguyen and Indraratna 2020a). A
226 perforated base plate with a 0.5 mm pore-opening size (1.5 times of the diameter of the largest
227 fine particle) is placed underneath each sample to allow the migration of the fine particles only.

228 3.4 Simulation procedure

229 A cuboid assembly of spheres was first generated randomly with the prescribed gradation
230 (Fig. 1) and compacted by six surrounding walls under the 50 kPa confinement. The inter-
231 particle friction coefficient was maintained at a relatively low value of 0.1 during the sample
232 preparation processes (i.e., generating particles and applying isotropic pressure to the sample)
233 to generate a relatively dense sample. After the sample preparation and before applying seepage
234 flow, the inter-particle friction coefficient is increased to 0.3.

235 After the generation of the initial DEM sample, a differential hydraulic pressure was
236 imposed on the upstream and downstream of the sample to model internal erosion.
237 Simultaneously, the dispersed suspension particles were generated periodically in the upstream
238 region. The information of each particle (including position, velocity and drag force) and
239 contact (including the positions of particles in contact and contact force) were recorded every
240 0.05 s during the entire simulation. Each simulation that models 15 seconds of physical time
241 of erosion in this study took approximately 5~7 days on an HP workstation with 8 Intel Xeon
242 E52680-v4 2.4GHz processors and 512GB DDR4 RAM. The simulation duration (i.e., 15 s) is
243 relatively short as compared to that in a laboratory test. Nevertheless, the numerical results
244 presented below show that this duration has largely covered the key stages for internal erosion
245 involved in each analysis, i.e., initiation and a gradually stabilized response. The key macro-
246 and microscopic mechanisms on the internal erosion of gap-graded soil are contained in each

247 simulation reported herein.

248 **4. Numerical results and discussion**

249 **4.1 Net cumulative fine particle loss**

250 Fig. 5(a) shows the percentage of the net cumulative fine particle loss ($m_{e_net}=m_e-m_{in}$,
251 where m_e and m_{in} denote the percentage by mass of the particles flowing out and into the sample,
252 respectively) for the samples with $F_c=15\%$ under different C and i . It is found that a higher
253 hydraulic gradient facilitates the internal erosion for the sample under the same concentration
254 because of larger drag forces applied to fine particles. The existence of the suspension particles
255 decreases the net fine particle loss compared with that in the case of $C=0$. This is because the
256 fine particles under-fill the voids between coarse particles for the sample with $F_c=15\%$, leading
257 to an easier occupation of the remaining space by the suspension particles. Higher suspension
258 concentration increases the influx of the suspension particles (the mass of suspension particles
259 through the unit cross-sectional area within a unit time), facilitating clogging at the top of the
260 sample and impeding the development of internal erosion. Figs. 5(b) and 5(c) show that the
261 development of the vertical and transverse strains of the sample with $F_c=15\%$ during erosion.
262 The transverse strain in this study is defined as the average value of the strain in two horizontal
263 directions (i.e., the ratio of the change in the width of the sample to its original width). The
264 sample deformations in different cases are slightly affected by the erosion of the fine particles
265 because the sample of $F_c=15\%$ is mainly composed of contacts between coarse particles.

266 Fig. 6 compares the cumulative eroded fine particle loss in the case of $i=0.25$ and $F_c=15\%$
267 under different concentrations and rolling friction. Although the incorporation of the rolling
268 friction decreases the eroded fine particle loss for each case, the trend for the eroded fine

269 particle loss under different concentrations is unchanged. In other words, it is reasonable to
270 assume that the effects of rolling friction and suspension concentration are independent.

271 Fig. 7(a) shows the percentage of the net cumulative fine particle loss (m_{e_net}) for the
272 sample with $F_c=35\%$. Comparing Fig. 5(a) to Fig. 7(a), the m_{e_net} of the sample with $F_c=35\%$
273 also increases with the hydraulic gradient but varies slightly under different suspension
274 concentrations. For the sample with a high fine fraction (e.g., $F_c=35\%$), the fine particles
275 overflow the voids between coarse particles, preventing the entry of the suspension particles to
276 the sample. Figs. 7(b) and 7(c) show the development of vertical and transverse strains of the
277 sample with $F_c=35\%$ during erosion. Although the m_{e_net} of the samples with $F_c=15\%$
278 ($m_{e_net}=0.6\%\sim 3.5\%$) is two or three times larger than that of the samples with $F_c=35\%$
279 ($m_{e_net}=0.75\%\sim 1.8\%$), the strain level of the former (i.e., $0.005\%\sim 0.16\%$) is much smaller than
280 that of the latter (i.e., $0.2\%\sim 1.6\%$) because of the different types of their material fabrics. For
281 the sample with $F_c=15\%$, the coarse particles are in contact with each other while most fine
282 particles are confined within voids between coarse particles, providing little support to the
283 coarse particles (Skempton and Brogan 1994; Minh et al. 2014; Shire et al. 2014). Thus, the
284 erosion of the fine particles has rarely affected the stability of the coarse particle supported
285 fabric which mainly carries the external pressure ($p'=50$ kPa in this study). For the sample with
286 $F_c=35\%$, however, the coarse particles are dispersed within a matrix of fine particles (Skempton
287 and Brogan 1994; Minh et al. 2014; Shire et al. 2014). Then the erosion of the fine particles
288 leads to the rearrangement of the coarse particles and hence a relatively large deformation of
289 the entire sample.

290 Fig. 8 shows the erosion rate in terms of mass percentage for the samples with $F_c=15\%$

291 and 35% under different suspension concentrations (C) and hydraulic gradients (i). For the
292 samples with $F_c=15\%$, the fine particles are susceptible to be eroded under a higher i and a
293 lower C . The suspension concentrations (C) have a slight influence on the erosion rate for the
294 sample with $F_c=35\%$, as similar to the behavior of cumulative eroded fine particle loss (Fig.
295 7(a)). The erosion rate for both samples under each condition is relatively larger at the
296 beginning of internal erosion and then gradually decreases until the end of the simulations. This
297 behavior is also observed in previous experiments (Chang 2012), which demonstrates the
298 predictive capability of the CFD-DEM method for capturing the main characteristics of internal
299 erosion in a limited simulation time (i.e., 15 s).

300 4.2 Vertical distribution of fine fraction

301 Fig. 9 shows the distribution of fine fraction along the height of the samples with $F_c=15\%$
302 and 35% after the action of seepage with different C and i . For the sample $F_c=15\%$ and $C=0$,
303 Fig. 9(a) shows that the fine fraction near the top of the sample is smallest compared with that
304 near the middle and bottom, suggesting that the fine particles near the top are dragged
305 downward by the seepage force. This phenomenon is consistent with the experimental
306 observations reported by Chang and Zhang (2013) and Nguyen et al. (2019). When the influent
307 contains the suspension particles ($C>0$ g/L), the fine fraction along the full height of the sample
308 increases due to the deposition of the suspension particles. However, the suspension particles
309 are mostly retained near the top of the samples.

310 Fig. 9(b) shows that the fine particles at the top of the sample with $F_c=35\%$ are eroded the
311 least in all cases. This is because the fine particles in this sample overflow the voids between
312 coarse particles, leading to a higher number of fine contacts with stronger contact forces than

313 the fine particles in the sample with $F_c=15\%$ (Shire et al. 2014), making the fine particles in
 314 the former less vulnerable to detachment and migration. Comparing to the fine particles near
 315 the top of the sample with $F_c=35\%$, the fine particles near its bottom (i.e., the outlet) are prone
 316 to be eroded as shown in Fig. 7(b). This also agrees with previous experimental findings
 317 (Valdes and Santamarina 2007; Bendahmane et al. 2008). A weak erosion of the fine particles
 318 at the top of this sample prevents the entry of the suspension particles, results in a slight increase
 319 of the fine fraction at the top region in the case with large concentrations ($C=30$ and 60 g/L).

320 4.3 Results on hydraulic conductivity

321 Figs. 10(a) and 10(b) show the evolution of the overall hydraulic conductivity for the
 322 whole samples with $F_c=15\%$ and 35% under different C and i , respectively. The hydraulic
 323 conductivity (k) considered in this study is defined as follows:

$$k = \frac{q}{Ai} \quad (2)$$

324 where q is the flow rate. i is the hydraulic gradient along with the sample height. A is the cross-
 325 section of the sample. Each value of instantaneous hydraulic conductivity k during erosion is
 326 normalized by the initial value k_0 of the corresponding sample before erosion. For the sample
 327 with $F_c=15\%$, its hydraulic conductivity increases with i . This is because higher i induces more
 328 fine particle loss (see Fig. 5(a)) and hence a larger increase of the void ratio or porosity. The
 329 porosity-dependent hydraulic conductivity has been well recognized and formulated in the
 330 literature, e.g., Scheidegger's formulation (Scheidegger 1958) that correlates porosity (ϕ) to
 331 soil hydraulic conductivity k , as follows:

$$k = \frac{C_s}{\tau^2 S_s^2} \frac{\phi^3}{(1-\phi)^2} \quad (3)$$

332 where C_s is the empirical shape factor, S_s is the specific surface area per grain volume, which
 333 is defined as the ratio between the total surface area ΣS_i and the total volume ΣV_i of particles
 334 in each sample. τ is the tortuosity ($=L_a/L$; where L_a is the average length of the fluid path, L is
 335 the geometrical length of the sample that fluid flows through), and ϕ is the soil porosity. The S_s
 336 and ϕ are calculated by the radius of the current particles in each sample which are directly
 337 output by the DEM code. The tortuosity in Eq. 3 is one of the most abused parameters due to
 338 the lack of understanding and the lack of proper ways to measure it. Therefore, hydraulic
 339 tortuosity is often treated merely as a fitting factor, or worse (Han et al. 2018). In this study,
 340 the tortuosity (τ) is estimated as follows:

$$\tau = \frac{\Delta L_a}{\Delta L} = \frac{\Delta L_a / \Delta t}{\Delta L / \Delta t} = \frac{\bar{v}_a}{v_D} \quad (4)$$

341 where ΔL_a and ΔL are the average path and the geometrical length of the sample that fluid flows
 342 through per unit time Δt , respectively. \bar{v}_a and v_D are the average pore flow velocity and
 343 Darcy flow velocity, respectively. \bar{v}_a is estimated by the average flow velocity of all the CFD
 344 cells. v_D equals q/A , where q is the flow rate obtained directly from the CFD code and A is
 345 the cross-section area of the sample. To evaluate the above approach for τ , the evolution of the
 346 values of τ calculated by Eq. 4 (this study) is compared with the results calculated by the
 347 method proposed by Nguyen and Indraratna (2020b) for each case. Eq. 5 is the equation
 348 proposed by Nguyen and Indraratna (2020b) to estimate the tortuosity of granular materials,
 349 which is derived from back-analysis based on experimental data.

$$\tau = p(1 - \ln(n)) \quad (5)$$

350 where n is the porosity of the sample, $p=0.6$ and 1.15 for spheres and natural sand. Considering
 351 that all particles in this study are spherical, $p=0.6$ is therefore adopted.

352 For the samples with $F_c=15\%$, Fig. 11(a) shows that the τ calculated by both the approach
353 in this study and that of Nguyen and Indraratna (2020b) in each case decreases during internal
354 erosion due to the fine particle loss and the accompanying increase of the sample porosity (n).
355 Besides, the decrease of τ estimated by the approach in this study is larger than that of Nguyen
356 and Indraratna (2020b). It is probably because Eq. 5 is derived from non-gap-graded soils and
357 thus unable to consider the contribution of the local erosion zone (see Fig. 12(a) and 12(b)) to
358 the decrease of τ . The scatters between the two methods exist because both of them are indirect
359 estimations of τ . Similarly, Fig. 11(b) shows that the τ for the samples with $F_c=35\%$ in each
360 case still decreases at the end of the internal erosion. The slight increase of τ at the initial stage
361 in the case of $i=0.10$ is primarily due to the clogging of the suspension particles at the top of
362 the samples.

363 Fig 10 shows the calculated hydraulic conductivity for each sample according to Kozeny-
364 Carman equation, i.e., Eq. 3. It can be seen that the equation has broadly captured the evolution
365 of hydraulic conductivity with the change of porosity resulting from the internal erosion in
366 different samples. Note that scatters between the calculated and the computed results could be
367 found due to the heterogeneity of the fine fraction and void ratio within the sample subjected
368 to internal erosion (Sterpi 2003; Sibille et al. 2015). On the other hand, the clogging area
369 (analyzed in the section below) within the sample possibly has a strong effect on the prevention
370 of the fluid flow and hence decreases the hydraulic conductivity further, which can't be
371 reflected in the theoretical equation.

372 4.4 Migration of fine particles and evolution of constriction size distribution

373 Fig. 12 shows the configuration of the sample packing and streamlines for the samples
374 with $F_c=15\%$ and $F_c=35\%$ under $i=0.25$ and $C=30$ g/L at the beginning and the end of the

375 simulation. For the sample with $F_c=15\%$, Figs. 12(a) and 12(b) show that the specific zones
376 where fine particles have been washed out completely (only the coarse particles remained)
377 develop from the top and then progress the downwards. This is consistent with the experimental
378 findings of Chang (2012) and Ke and Takahashi (2014). It is worth noting that the flow in the
379 erosion zone, as shown in the black square frame in Fig. 12(b), has a larger flow velocity due
380 to larger void space compared with that of the surrounding zone. The erosion amount in the
381 region is also larger, suggesting that the fine particles are eroded through an erosion channel
382 rather than uniformly pass through a transection of the sample. This is usually caused by a
383 partial clogging of the interstitial space outside the erosion channel (Sterpi 2003; Sibille et al.
384 2015). The streamlines in Fig. 12 (b) show that the fluid flow within the sample with $F_c=15\%$
385 has a significant heterogeneity in terms of flow velocity and direction at the end of the
386 simulation, which is caused by the inhomogeneous distribution of the fine particles within the
387 sample. Fig. 12 (b) also shows the average fluid velocity of the fluid cells along with the sample
388 height. At the height with erosion region, as shown in the black frame, the average fluid velocity
389 is correspondingly larger, which is consistent with the results presented by the streamlines in
390 Fig. 12 (b).

391 Figs. 12(c) and 12(d) show that for the sample with $F_c=35\%$, the inhomogeneous
392 migration of the fine particles is less apparent at the end of the simulation compared with that
393 of the sample with $F_c=15\%$. The reason for this phenomenon includes two aspects. First, the
394 detachment of the fine particles is restricted due to stronger contact forces and a higher number
395 of contacts between the fine particles. On the other hand, the overfilled voids between the
396 coarse particles leave small space for free migration of the fine particles, preventing their

397 gradual accumulation in a local zone and hence the occurrence of clogging. Due to a relatively
398 uniform fine particle distribution, the fluid flow within the sample is also relatively uniform in
399 terms of flow velocity and direction at the beginning and the end of the erosion process.

400 Previous researches (Indraratna et al. 2007; Indraratna et al. 2015) reveal that the
401 constriction size (diameter of the constriction constituted by the coarse particles) formed by
402 the coarse particles controls the detachment, migration and clogging of fine particles. A
403 criterion based on the constriction size distribution constituted by the coarse particles is also
404 proposed to evaluate the internal erosion for granular filters (Indraratna et al. 2007). In this
405 study, the constriction size is calculated by the method proposed by Shire and O'Sullivan
406 (2016). This method first partitions the sample using a three dimensional weighted Delaunay
407 tessellation with the tetrahedra vertices being located at the particle centroids. On each
408 tessellation face the constriction size is then assumed to be the diameter of the circle that can
409 be inscribed between particles. If two inscribed circles overlap to some extent, they are merged
410 and deemed as a constriction (Shire and O'Sullivan 2016).

411 Fig. 13 shows the evolution of the distribution of the constriction size formed by the coarse
412 and fine particles in the erosion and clogging areas in the case of $F_c=15\%$, $i=0.25$ and $C=60$
413 g/L. The insets of Figs. 12(a) and 12(b) show the evolution of the local packing configuration
414 for the erosion and clogging areas, respectively. In the erosion area (Fig. 13(a)), the fine
415 particles are gradually lost while coarse particles remain stationary in the erosion process. In
416 contrary to the erosion area, the fine particles gradually accumulate within the voids between
417 three or four coarse particles in the clogging area (Fig. 13(b)). The probability of the small
418 constriction size increases gradually in the clogging area but decreases in the erosion area

419 during erosion, which is consistent with the evolution of the local packing configurations for
 420 these two areas, as shown in the insets of Fig. 13.

421 4.5 Micromechanical analysis on clogging

422 The micromechanical analysis on the clogging phenomenon caused by suspension
 423 particles enables a better understanding of the macro observations, i.e., the cumulative fine
 424 particle loss and the deformation of the samples under different C (Figs. 5 and 7). It is also
 425 beneficial to reveal new insights into internal erosion with the suspension concentration. Fig.
 426 13(b) shows that in the clogging area, the fine particles are gradually accumulated and formed
 427 as a cluster. The fine particles in a cluster have a larger coordination number, which contributes
 428 to preventing the detachment and migration of these particles. The coordination number is
 429 defined in Eq. 6, as follows:

$$Z = \sum_{i=1}^{N_p} \left(\frac{C_i}{N_p} \right) \quad (6)$$

430 where C_i is the number of contacts between particle i and other particles; N_p is the total number
 431 of particles. On the other hand, the size of the cluster is also larger than the diameter of the
 432 voids between coarse particles, which contributes to the resistance of both the entire cluster
 433 and single fine particle to internal erosion. To quantify the micro-parameters of the cluster, Fig.
 434 14 compares the coordination number and the number density of the fine particles (i.e., the
 435 number of the fine particles per unit volume within the sample) in the cluster (Fig. 12(b)) and
 436 the entire sample. During internal erosion, the coordination number and the number density of
 437 the fine particles in the cluster are both larger compared with the mean value of the sample.
 438 These microscopic properties of the cluster validate previous analyses on its clogging

439 mechanism.

440 Considering that most of the suspension particles are retained near the top of the sample,
 441 the top region with a height of 10 mm (about the two-fifths height of the sample) is divided
 442 into eight sub-regions, as shown in the inset of Fig. 14. The retention ratio of the fine particles
 443 (R_{ret}) is used here to characterize the degree of clogging in each sub-zone, which is defined as
 444 follows:

$$R_{ret} = \frac{N_{pc}}{N_{pt}} \quad (7)$$

445 where N_{pc} is the number of the suspension particles retained in a region after erosion. N_{pt}
 446 is the total number of the suspension particles that flow through a region in the entire process
 447 of erosion. The coefficient of variation (i.e., the ratio of the standard deviation to the mean) for
 448 the constriction sizes of the eight sub-regions is about 0.01, suggesting that the packing in these
 449 selected regions is relatively uniform. However, the retention ratios R_{ret} of the eight sub-regions
 450 are quite different (varying from 0.48 to 0.79), implying that the mean constriction size alone
 451 is insufficient to determine whether the suspension particle would be retained or eroded.

452 Fig. 15 shows the initial constriction size distribution constituted by the coarse particles
 453 and the retention ratio in each sub-region. A statistical parameter, i.e., the cumulative
 454 probability of the mean constrictions (P_{mean}), is proposed in this study to analyze the influence
 455 of the constriction size distribution on the retention ratio. Generally, Fig. 15 shows that the fine
 456 particles are prone to be retained in the sub-region with a larger P_{mean} . This is because the fine
 457 particles have a larger probability to flow through a small constriction in a region with a larger
 458 P_{mean} and hence to plug or bridge at the small constriction. A gradual decrease of the

459 constriction size caused by the clogging of the fine particles in turn leads to more retention of
460 the fine particles flowing through the sub-region. It is also revealed from the figure that a slight
461 heterogeneity of the initial constriction size distributions in different regions can lead to quite
462 different mechanical responses during the internal erosion.

463 Nevertheless, the R_{ret} in each sub-region is not only determined by its initial constriction
464 size distribution. For instance, the region B2 has the smallest $P_{\text{mean}}=66\%$ but its R_{ret} is much
465 larger than region B1 and B4 with $P_{\text{mean}}=68\%$. Fig. 17 shows a schematic contour of R_{ret} for
466 the eight sub-regions, considering the P_{mean} and the suspension concentration. Although the
467 suspension particles are distributed uniformly in the influent, as shown in Fig. 4, the number
468 of suspension particles in each sub-region varies due to the heterogeneous fluid flow and
469 tortuosity (Moffat et al. 2011; Bacchin et al. 2014). Therefore, the suspension concentration in
470 each sub-region is defined as the time-average concentration in the entire erosion process. It
471 can be observed that the sub-regions with a smaller P_{mean} may experience a higher R_{ret} , because
472 of a higher concentration of the suspension flow in these sub-regions.

473 Fig. 17(a) shows the distribution of the suspension particles, the particle-fluid interaction
474 forces applied to them, and the streamlines in the case of $F_c=15\%$, $C=70$ g/L, and $i=0.25$ at the
475 end of erosion. The suspension particles at the bottom of the sample (i.e., the particles with a
476 larger migrated distance) are subjected to comparatively larger particle-fluid interaction forces.
477 Conversely, for the suspension particles clogged at the top of the sample, the particle-fluid
478 interaction forces applied to them are smaller. These results suggest that the suspension
479 particles subjected to larger particle-fluid interaction forces are more likely to migrate longer
480 distances while the particles subjected to smaller particle-fluid interaction forces probably

481 accumulate together (i.e., form cluster) and lead to the occurrence of clogging. The particle-
482 fluid interaction force on a particle is determined by the flow velocity of the fluid around it, as
483 shown in the streamlines in Fig. 17(a). The particles with larger particle-fluid interaction forces
484 are usually located in a region with larger flow velocity. The heterogeneous evolution of the
485 flow velocity within the sample may be affected by a slight difference in the initial constriction
486 size distribution and fine particle distribution among different sub-regions, which is an
487 interesting topic and will be analyzed in the future work.

488 To quantitatively address the influences of the hydraulic drag forces acting on particles on
489 soil migration, Fig. 17(b) shows the relationship between the particle-fluid interaction force
490 averaged over time and migration distance for the suspension particles. Most suspension
491 particles subjected to larger particle-fluid interaction force migrate longer within the sample,
492 which is consistent with the results as shown in Fig. 17(b).

493 5. Conclusions

494 This paper presents the micro-macro investigation from a 3D coupled CFD-DEM analysis
495 of internal erosion in gap-graded granular soils, with particular consideration of suspension
496 flow. Two typical gradations, i.e., samples under-filled and overfilled with fine particles (fine
497 fraction $F_c=15$ and 35%, respectively), were considered under the conditions of different
498 hydraulic gradients and suspension concentrations. Micro-scale variables were studied to
499 investigate the influence of the suspension concentration on the internal erosion behavior of
500 soils and the occurrence of clogging. Based on the analyses of all simulation results, the
501 following conclusions can be made:

502 (1) For the sample under-filled with fine particles ($F_c=15\%$), the suspension flow

503 decreases the cumulative eroded fine particle loss and the increasing rate of soil hydraulic
504 conductivity due to clogging near the top of the sample. For the sample with $F_c=35\%$, the fine
505 particles overflow the voids between coarse particles, preventing the entry of the suspension
506 particles to the sample. In this case, the suspension flow has slight influences on the erosion
507 behavior of the sample.

508 (2) Due to the heterogeneous nature of internal erosion, a slight heterogeneity of the initial
509 constriction size distributions in different regions can lead to quite different mechanical
510 responses during the internal erosion for different sub-regions, i.e., the formation of the erosion
511 area and clogging area. The probability of the small constriction size increases gradually in the
512 clogging area but decreases in the erosion area during erosion.

513 (3) The clogging degree, characterized by the retention ratio, is found to depend on both
514 the constriction size distribution and the suspension concentration. A big cumulative
515 probability of the mean constriction size (P_{mean}) facilitates the capture of suspension particles.
516 A high suspension concentration in internal erosion increases the probability of the contacts
517 between suspension particles, which also contributes to the capture of the particles and
518 facilitates the occurrence of clogging.

519 (4) The particles in a cluster have a high resistance to the drag force exerted by the fluid
520 flow. Firstly, the fine particles in a cluster have a larger coordination number than that of the
521 fine particles outside the cluster, which helps to stabilize the fine particles in the cluster.
522 Secondly, the size of a cluster is much larger than the diameter of the voids between the coarse
523 particles, preventing further migration of the fine particles.

524 **Acknowledgement**

525 The work presented in this paper is supported by the GRF project (Grant No. 15209119)
526 from Research Grants Council (RGC) of Hong Kong. National Key Research and Development
527 Program of China (2016YFC0800200) and National Natural Science Foundation of China
528 (51939010 and 51779221).
529

Draft

530 **References**

- 531 Amir, Z., and Brij, M. 2009. Flow of dispersed particles through porous media-Deep bed
532 filtration. *Journal of Petroleum Science and Engineering*, **69**(1):71-88.
- 533 Alem, A., Ahfir, N.D., Elkawafi, A., and Wang, H.Q. 2015. Hydraulic Operating Conditions
534 and Particle Concentration Effects on Physical Clogging of a Porous Medium. *Transport*
535 *in Porous Media*, **106**(2):303-321.
- 536 Bacchin, P., Derekx, Q., Veyret, D., Glucina, K., and Moulin, P. 2014. Clogging of microporous
537 channels networks: role of connectivity and tortuosity. *Microfluid Nanofluid*, **17**(1):85-
538 96.
- 539 Bendahmane, F., Marot, D., and Alexis, A. 2008. Experimental parametric study of suffusion
540 and backward erosion. *Journal of Geotechnical and Geoenvironmental Engineering*,
541 **134**(1):57-67.
- 542 Benamar, A., Santos, R.N.C., Bennabi, A., and Karoui, T. 2019. Suffusion evaluation of coarse-
543 graded soils from Rhine dikes. *Acta Geotechnica*, **14**(3):815-823.
- 544 Burenkova, V.V. 1993. Assessment of Suffusion in Non-Cohesive and Graded Soils. *In*
545 *Proceedings of the 1st International Conference "Geo-Filters", Filters in Geotechnical*
546 *Engineering*, Balkema, pp. 357-360.
- 547 Chang, D.S., and Zhang, L.M. 2013. Critical Hydraulic Gradients of Internal Erosion under
548 Complex Stress States. *J. Geotech. Geoenvironmental. Eng.*, **139**(9):1454-1467.
- 549 Chang, D.S. 2012. Internal erosion and overtopping erosion of earth dams and landslide dams.
550 PhD thesis, Hong Kong University of Science and Technology, Hong Kong.
- 551 Goldsztein, G.H. 2005. Volume of suspension that flows through a small orifice before it clogs.
552 *SIAM J. APPL. MATH*, **66**(1):228-236.
- 553 Goniva, A., Kloss, C., Deen, N.G., Kuipers, J.A.M., and Pirker, S. 2012. Influence of rolling
554 friction on single spout fluidized bed simulation. *Particuology*, **10**(5):582-591.
- 555 Han, G., Kwon, T.H., Lee, J.Y., and Kneafsey, T.J. 2018. Depressurization-induced fines
556 migration in sediments containing methane hydrate: X-Ray computed tomography
557 imaging experiments. *Journal of Geophysical Research: Solid Earth*, **123**(4):2539-2558.
- 558 Hicher, P-Y. 2013. Modelling the impact of particle removal on granular material behavior.
559 *Géotechnique*, **63**(2):118-128.
- 560 Hu, Z., Zhang, Y.D., and Yang, Z.X. 2019. Suffusion-induced deformation and microstructural
561 change of granular soils: a coupled CFD-DEM study. *Acta Geotechnica*, **14**(3):795-814.
- 562 Indraratna, B., Raut, A., and Khabbaz, H. 2007. Constriction-based retention criterion for
563 granular filter design. *Journal of Geotechnical and Geoenvironmental Engineering*,
564 **133**(3):266-276.
- 565 Indraratna, B., Israr, J., and Rujikiatkamjorn, C. 2015. Geometrical Method for Evaluating the
566 Internal Instability of Granular Filters Based on Constriction Size Distribution. *Journal of*
567 *Geotechnical and Geoenvironmental Engineering*, **141**(10):04015045.

- 568 Israr, J., and Indraratna, B. 2019. Study of critical hydraulic gradients for seepage-induced
569 failures in granular soils. *Journal of Geotechnical and Geoenvironmental Engineering*,
570 **145**(7): 04019025.
- 571 Jasak, H., Jemcov, A., and Tukovic, Z. 2007. OpenFOAM: A C++ library for complex physics
572 simulations. *In Proc., Int. Workshop on Coupled Methods in Numerical Dynamics*.
573 Dubrovnik, Croatia, pp. 1000.
- 574 Ke, L., and Takahashi, A. 2015. Drained monotonic responses of suffusional cohesionless soils.
575 *Journal of Geotechnical and Geoenvironmental Engineering*, **141**(8): 04015033.
- 576 Kawano, K., Shire, T., and O'Sullivan, C. 2018. Coupled particle-fluid simulations of the
577 initiation of suffusion. *Soils and Foundations*, **58**(4):972-985.
- 578 Kloss, C., Goniva, C., Hager, A., Amberger, S., and Pirker, S. 2012. Models, algorithms and
579 validation for opensource DEM and CFD-DEM. *Prog. Comput. Fluid. Dyn. Int. J.*,
580 **12**(2):140-152.
- 581 Kezdi, A. 1979. *Soil physics-selected topics*. Elsevier Scientific Publishing Co. Amsterdam.
- 582 Li, M. 2008. Seepage induced instability in widely graded soils. Ph.D. thesis, Univ. of British
583 Columbia, Vancouver, BC, Canada.
- 584 Marot, D., Regazzoni, P.L., and Wahl, T. 2011. Energy-based method for providing soil surface
585 erodibility rankings. *Journal of Geotechnical and Geoenvironmental Engineering*,
586 **137**(12):1290-1293.
- 587 Moffat, R., Fannin, R.J., and Garner, S.J. 2011. Spatial and temporal progression of internal
588 erosion in cohesionless soil. *Canadian Geotechnical Journal*, **48**(3):399-412.
- 589 Minh, N.H., Cheng, Y.P., and Thornton, C. 2014. Strong force networks in granular mixtures.
590 *Granular Matter*, **16**(1):69-78.
- 591 Mindlin, R.D., and Deresiewicz, H. 1953. Elastic spheres in contact under varying oblique
592 forces. *Transactions of ASME, Series E. Journal of Applied Mechanics*, **20**:327-344.
- 593 Nguyen, C.D., Nadia, B., Edward, A., Luc, S., and Pierre, P. 2019. Experimental investigation
594 of microstructural changes in soils eroded by suffusion using X-ray tomography. *Acta*
595 *Geotechnica*, **14**(3):749-765.
- 596 Nguyen, T.T., and Indraratna, B. 2020a. A coupled CFD-DEM approach to examine the
597 hydraulic critical state of soil under increasing hydraulic gradient. *ASCE International*
598 *Journal of Geomechanics*, **20**(9):04020138-1:15.
- 599 Nguyen, T.T., and Indraratna, B. 2020b. The role of particle shape on hydraulic conductivity
600 of soils based on Kozeny-Carman approach. *Géotechnique Letters*, **10**(3):1-15.
- 601 Reddi, L.N., Xiao, M., Hajra, M.G., and Lee, I.M. 2005. Physical clogging of soil filters under
602 constant flow rate versus constant head. *Canadian Geotechnical Journal*, **42**(3):804-811.
- 603 Renzo, A.D., and Maio, F.P.D. 2004. Comparison of contact-force models for the simulation of
604 collisions in DEM-based granular flow codes. *Chemical Engineering Science*, **59**(3):525-
605 541.

- 606 Santos, R.N.C., Caldeira, L.M.M.S., and Neves, E.M. 2015. Experimental study on crack
607 filling by upstream fills in dams. *Géotechnique*, **65**(3):218-230.
- 608 Skempton, A.W., and Brogan, J.M. 1994. Experiments on piping in sandy gravels.
609 *Géotechnique*, **44**(3):449-460.
- 610 Sibille, L., Marot, D., and Sail, Y. 2015. A description of internal erosion by suffusion and
611 induced settlements on cohesionless granular matter. *Acta Geotechnica*, **10**(6):735-748.
- 612 Sterpi, D. 2003. Effects of the erosion and transport of fine particles due to seepage flow.
613 *International Journal of Geomechanics*, **3**(1):111-122.
- 614 Shire, T., O'Sullivan, C., Hanley, K.J., and Fannin, R.J. 2014. Fabric and effective stress
615 distribution in internally unstable soils. *Journal of Geotechnical and Geoenvironmental
616 Engineering*, **140**(12):04014072.
- 617 Shire, T., and O'Sullivan, C. 2016. Constriction size distributions of granular filters: a
618 numerical study. *Géotechnique*, **66**(10):826-839.
- 619 Scheidegger, A.E. 1958. *The Physics of Flow Through Porous Media*. University of Toronto
620 Press, Toronto.
- 621 Valdes, J.R., and Santamarina, J.C. 2007. Particle transport in a nonuniform flow field:
622 retardation and clogging. *Applied Physics Letters*, **90**(24):244101-244101-3.
- 623 Valdes, J.R., and Liang, S.H. 2006. Stress-controlled filtration with compressible particles.
624 *Journal of Geotechnical and Geoenvironmental Engineering*, **132**(7):861-868.
- 625 Wang, J., and Gutierrez, M. 2010. Discrete element simulations of direct shear specimen scale
626 effects. *Géotechnique*, **60**(5):395-409.
- 627 Wautier, A., Bonelli, S., and Nicot, F. 2018. Flow impact on granular force chains and induced
628 instability. *Physical Review E*, **98**(4):042909.
- 629 Wautier, A., Bonelli, S., and Nicot, F. 2019. DEM investigations of internal erosion: Grain
630 transport in the light of micromechanics. *International Journal for Numerical and
631 Analytical Methods in Geomechanics*, **43**(1):339-352.
- 632 Yang, Y., Cheng, Y.M., and Sun, Q.C. 2017. The effects of rolling resistance and non-convex
633 particle on the mechanics of the undrained granular assemblies in 2D. *Powder Technology*.
634 **318**(1):528-542.
- 635 Yang, J., Yin, Z-Y, Laouafa, F., and Hicher, P-Y. 2019. Internal erosion in dike-on-foundation
636 modeled by a coupled hydro-mechanical approach. *International Journal for Numerical
637 and Analytical Methods in Geomechanics*, **43**(3):663-683.
- 638 Yang, J., Yin, Z-Y, Laouafa, F., and Hicher, P-Y. 2020. Hydro-mechanical modeling of granular
639 soils considering internal erosion. *Canadian Geotechnical Journal*, **57**(2):157-172.
- 640 Yin, Z-Y, Zhao, J., and Hicher, P-Y. 2014. A micromechanics-based model for sand-silt
641 mixtures. *International Journal of Solids and Structures*, **51**(6):1350-1363.
- 642 Yin, Z-Y, Huang, H.W., and Hicher, P-Y. 2016. Elastoplastic modeling of sand-silt mixtures.
643 *Soils and Foundations*, **56**(3):520-532.

- 644 Zamani, A., and Maini, B. 2009. Flow of dispersed particles through porous media-Deep bed
645 filtration. *Journal of Petroleum Science and Engineering*, **69**(1):71-88.
- 646 Zheng, X.L., Shan, B.B., Chen, L., Sun Y.W., and Zhang S.H. 2014. Attachment-detachment
647 dynamics of suspended particle in porous media: Experiment and modeling. *Journal of*
648 *Hydrology*, **511**:199-204.
- 649 Zhang, F.S., Li, M., Peng, M., Chen, C., and Zhang, L. 2019. Three-dimensional DEM
650 modeling of the stress-strain behavior for the gap-graded soils subjected to internal
651 erosion. *Acta Geotechnica*, **14**:487-503.
- 652 Zhao, J., and Shan, T. 2013. Coupled CFD-DEM simulation of fluid-particle interaction in
653 geomechanics. *Powder Technology*, **239**:248-258.
- 654 Zhao, T., Uteri, S., and Crosta, G.B. 2016. Rockslide and impulse wave modelling in the Vajont
655 reservoir by DEM-CFD analyses. *Rock Mechanics and Rock Engineering*, **49**: 2437-2456.
- 656 Zhou, Y.C., Wright, B.D., Yang, R.Y., Xu, B.H., and Yu, A.B. 1999. Rolling friction in the
657 dynamic simulation of sandpile formation. *Phys A Stat Mech Appl*, **269**:536-553.

Draft

Tables

Table 1 Simulation program and the number of particles in each sample

Simulation identity	Fine fraction, F_c (%)	Suspension concentration, C (g/L)	Hydraulic gradient, i	No. of total particles	No. of coarse particles	No. of fine particles				
FC15C0L		0	0.1							
FC15C30L		30	0.1							
FC15C60L	15	60	0.1	27287	697	26590				
FC15C0H		0	0.25							
FC15C30H		30	0.25							
FC15C60H		60	0.25							
FC35C0L			0				0.1			
FC35C30L			30				0.1			
FC35C60L	35	60	0.1	55203	479	54724				
FC35C0H		0	0.25							
FC35C30H		30	0.25							
FC35C60H		60	0.25							

Table 2 Summary of model parameters

	Model parameters	Values for the validation model	Values for the model with suspension flow
Physical model	Sample dimensions $L \times W \times H$ (mm)	13×13×13	13×13×26
	Simulation time (s)	40.0	15.0
CFD	Cells	5×5×6	5×5×12
	Fluid viscosity, μ (Pa·s)	1×10^{-3}	1×10^{-3}
	Density, ρ (kg/m ³)	1000	1000
	Time step (s)	1×10^{-4}	1×10^{-4}
DEM	Elastic modulus, E (Pa)	7×10^9	7×10^9
	Poisson's ratio, ν	0.3	0.3
	Coefficient of Restitution, e	0.7	0.7
	Friction coefficient, μ_f	0.5	0.5
	Rolling friction coefficient, μ_r	0.1	0.1
	Time step (s)	5×10^{-7}	5×10^{-7}

Caption of Figures

- Figure 1 Grain size distribution of the soils in this study and the experiment of Chang (2012)
- Figure 2 Erosion behavior of the sample with $F_c=35\%$: (a) cumulative eroded soil weight percentage under $p'=50$ and 200 kPa; (b) sample deformations under $p'=50$ kPa; (c) sample deformations under $p'=200$ kPa
- Figure 3 Assessment of internal stability for the samples with $F_c=15\%$ and 35% by Burenkova method
- Figure 4 Model setup
- Figure 5 Simulation results for the samples with $F_c=15\%$ under different hydraulic gradient and suspension concentration: (a) cumulative eroded soil weight percentage; (b) vertical strain; (c) transverse strain
- Figure 6 Cumulative eroded soil weight percentage in the case of $i=0.25$ and $F_c=15\%$ under different concentrations and rolling friction
- Figure 7 Simulation results for the samples with $F_c=35\%$ under different hydraulic gradient and suspension concentration: (a) cumulative eroded soil weight percentage; (b) vertical strain; (c) transverse strain
- Figure 8 Erosion rate in terms of mass percentage for the samples with (a) $F_c=15\%$ and (b) $F_c=35\%$ under different suspension concentrations (C) and hydraulic gradients (i)
- Figure 9 Distribution of the fine fraction after erosion along the height of the sample with (a) $F_c=15\%$ (b) $F_c=35\%$
- Figure 10 Evolution of the hydraulic conductivity for the sample with (a) $F_c=15\%$ and (b) $F_c=35\%$ (k_0 of the sample with $F_c=15\%$ and 35% are 3.6×10^{-4} cm/s and 1.8×10^{-4} cm/s, respectively)
- Figure 11 Comparison of the tortuosity (τ) calculated by the approach of this study with that of Nguyen and Indraratna (2020(b)) for the samples with (a) $F_c=15\%$ and (b) $F_c=35\%$
- Figure 12 Interaction between fine migration and fluid flow at the (a) initial time and (b) end of the simulation for the sample with $F_c=15\%$ and (c) initial time and (d) end of the simulation for the sample with $F_c=35\%$ under $i=0.25$ and $C=30$ g/L
- Figure 13 Evolution of the local packing configuration and constriction size distribution for the (a) erosion area and (b) clogging area
- Figure 14 (a) Cluster formed by suspension particles at the top of the sample; (b) coordination number and number density of the fine particles in the cluster and the entire sample

- Figure 15 Relationship between the constriction size distribution and the retention ratio for (a) region A; (b) region B
- Figure 16 Assessment of the retention ratio based on P_{mean} and concentration (normalized by the average concentration of the eight sub-zones)
- Figure 17 Relationship between the average particle-fluid interaction force during erosion and migration distance for the suspension particles in the case of $F_c=15\%$, $C=70$ g/L, and $i=0.25$ (a) at the end of erosion; (b) during internal erosion

Draft

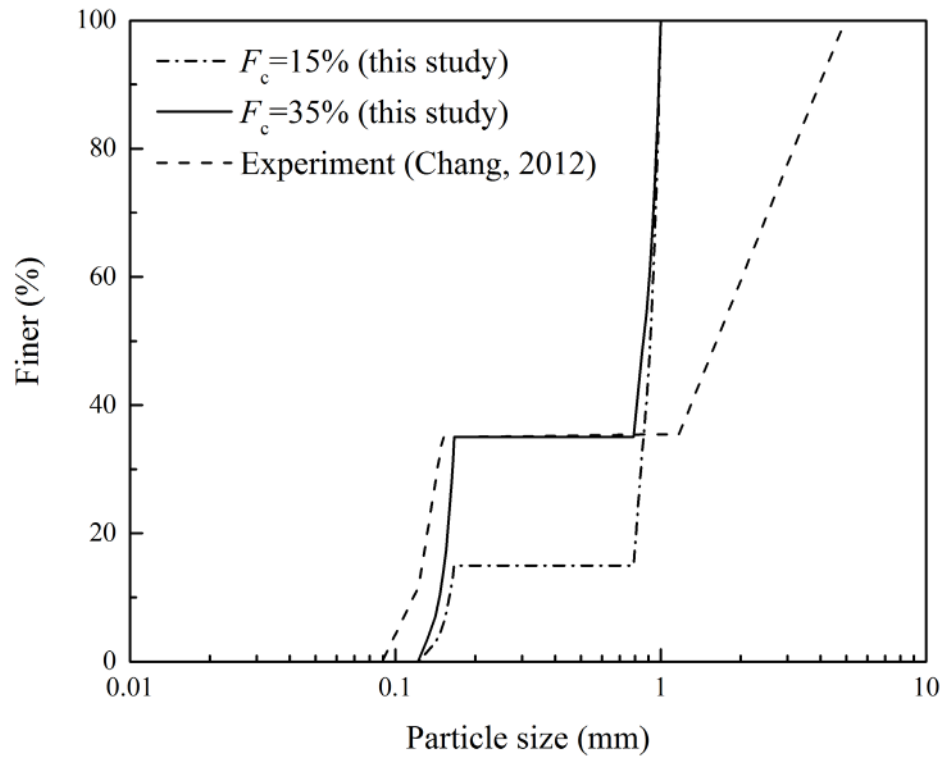


Figure 1 Grain size distribution of the soils in this study and the experiment of Chang (2012)

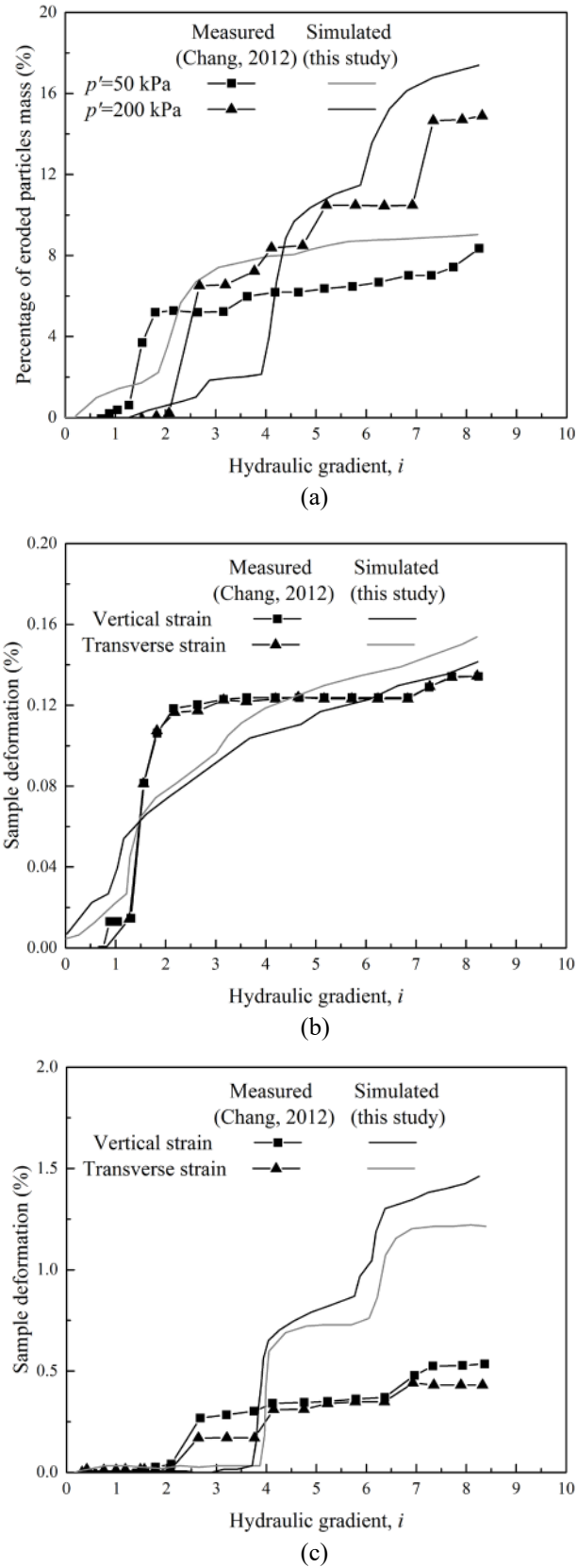


Figure 2 Erosion behavior of the sample with $F_c=35\%$: (a) cumulative eroded soil weight percentage under $p'=50$ and 200 kPa; (b) sample deformations under $p'=50$ kPa; (c) sample deformations under $p'=200$ kPa

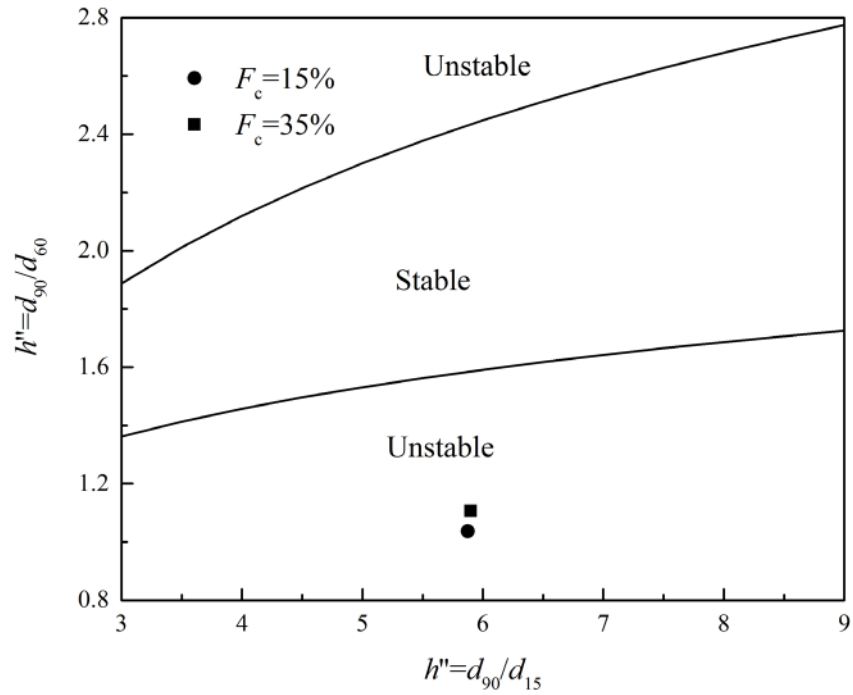


Figure 3 Assessment of internal stability for the samples with $F_c=15\%$ and 35% by Burenkova method

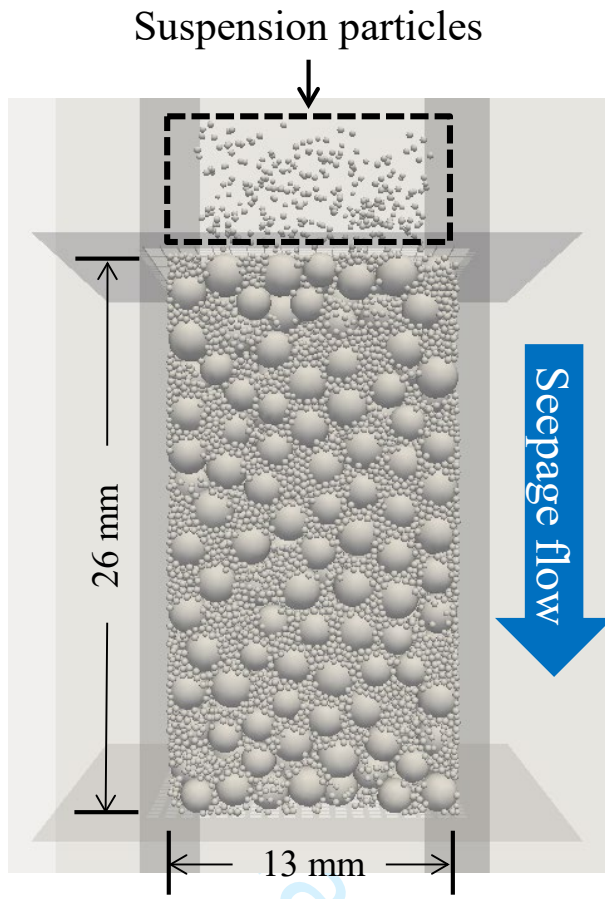


Figure 4 Model setup

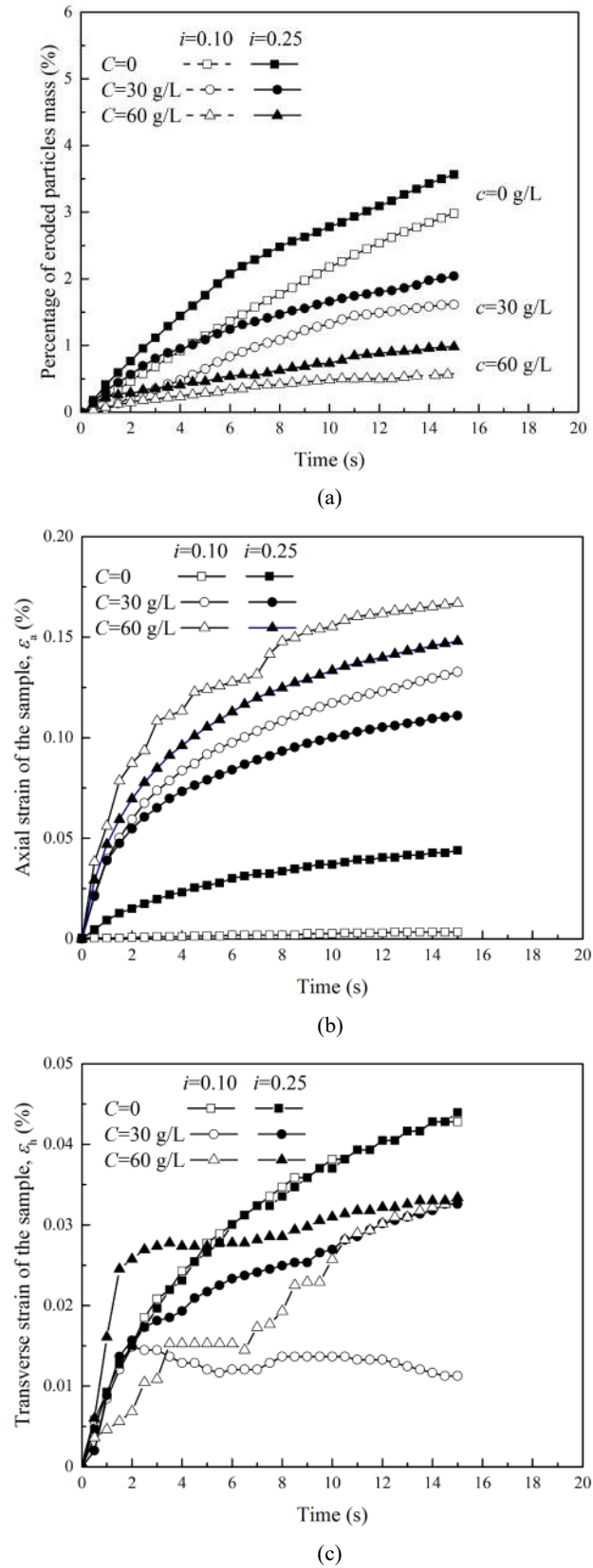


Figure 5 Simulation results for the samples with $F_c=15\%$ under different hydraulic gradient and suspension concentration: (a) cumulative eroded soil weight percentage; (b) vertical strain; (c) transverse strain

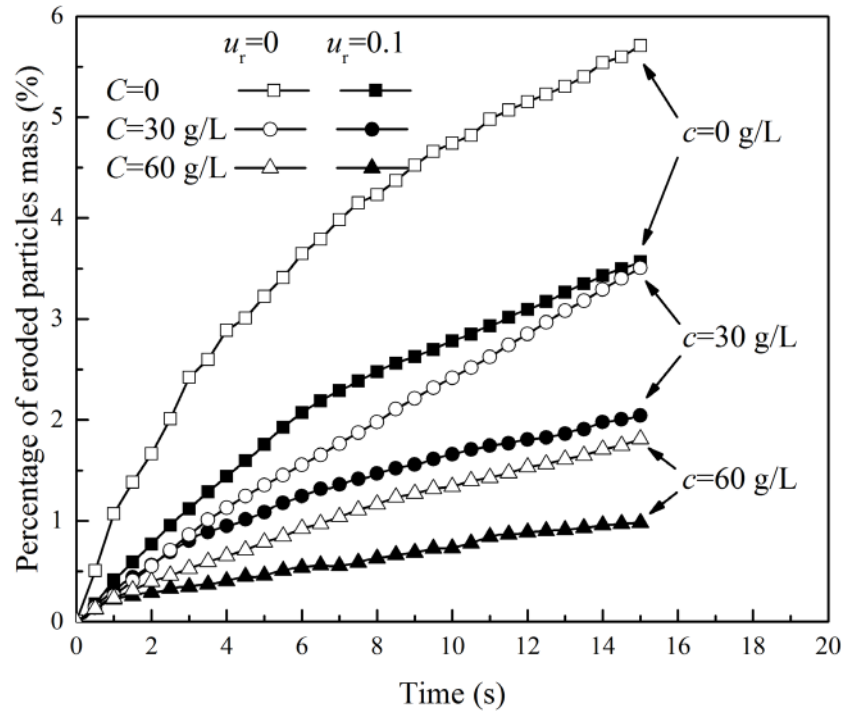


Figure 6 Cumulative eroded soil weight percentage in the case of $i=0.25$ and $F_c=15\%$ under different concentrations and rolling friction

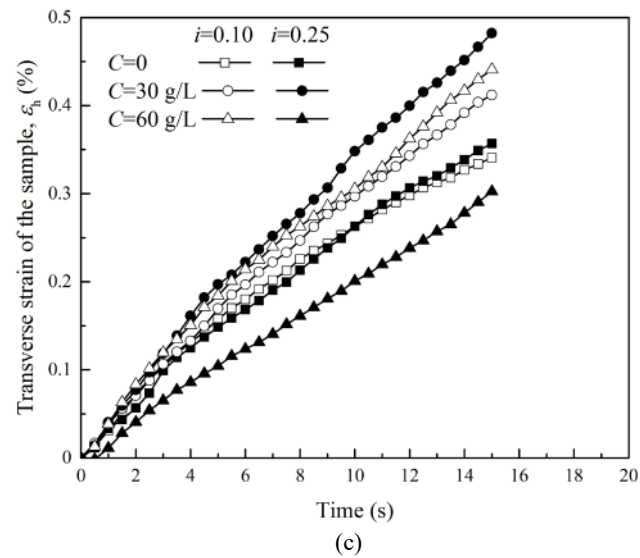
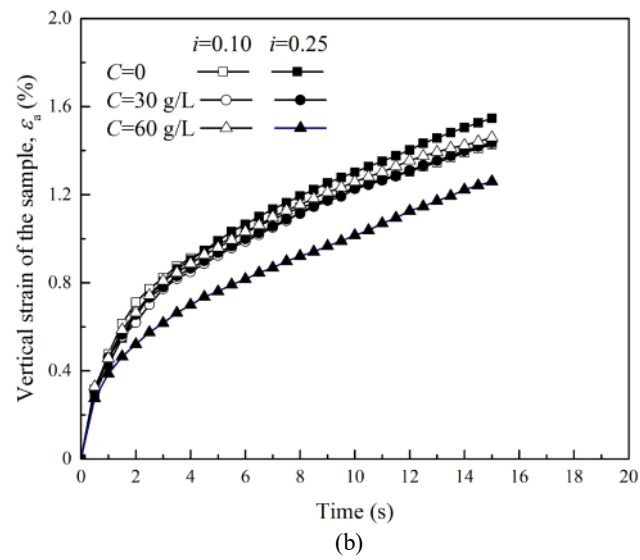
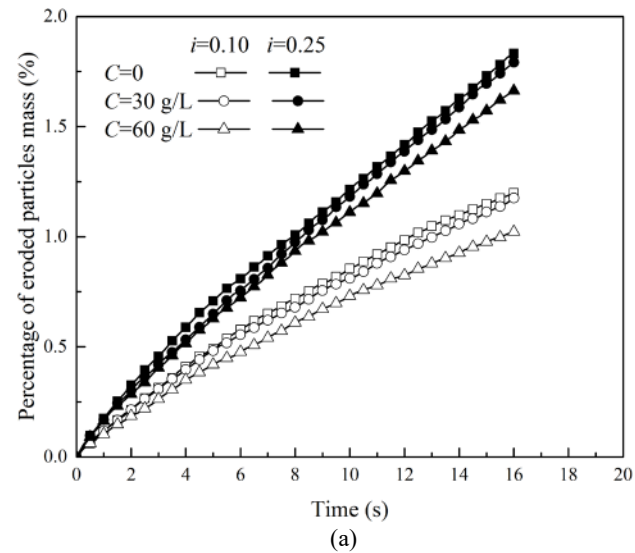


Figure 7 Simulation results for the samples with $F_c=35\%$ under different hydraulic gradient and suspension concentration: (a) cumulative eroded soil weight percentage; (b) vertical strain; (c) transverse strain

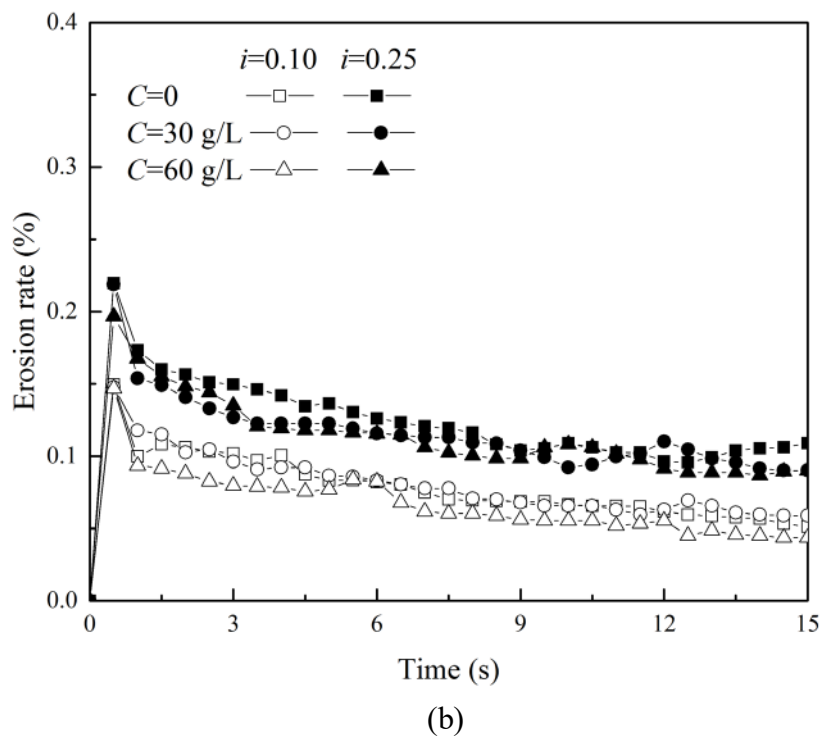
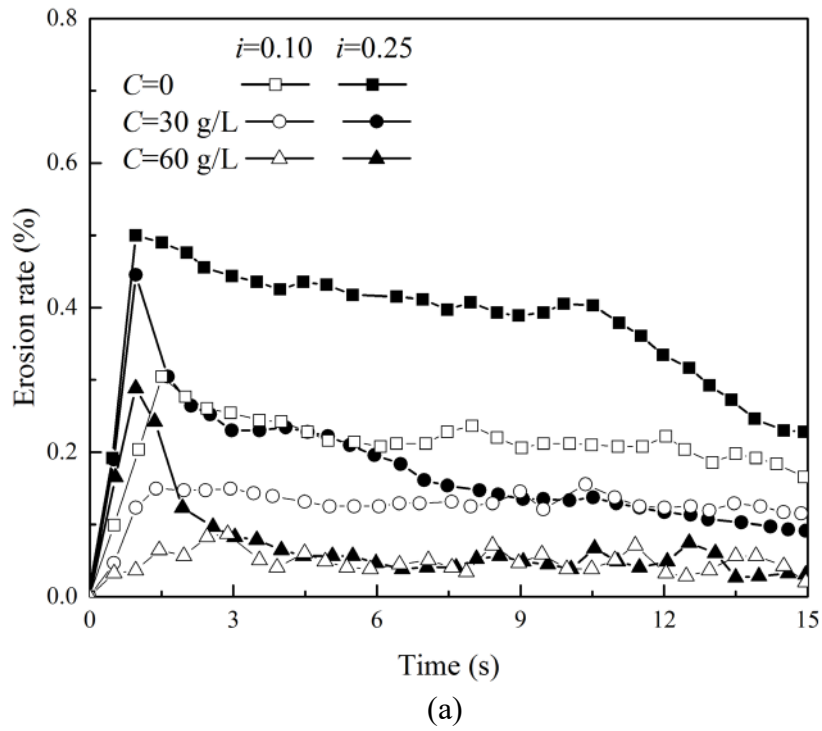
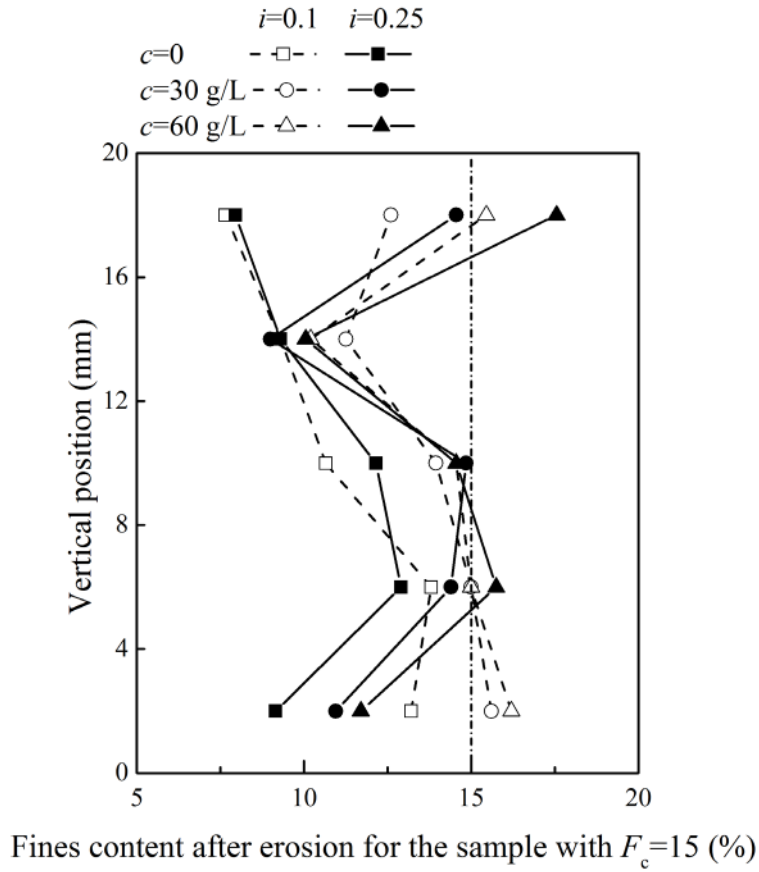
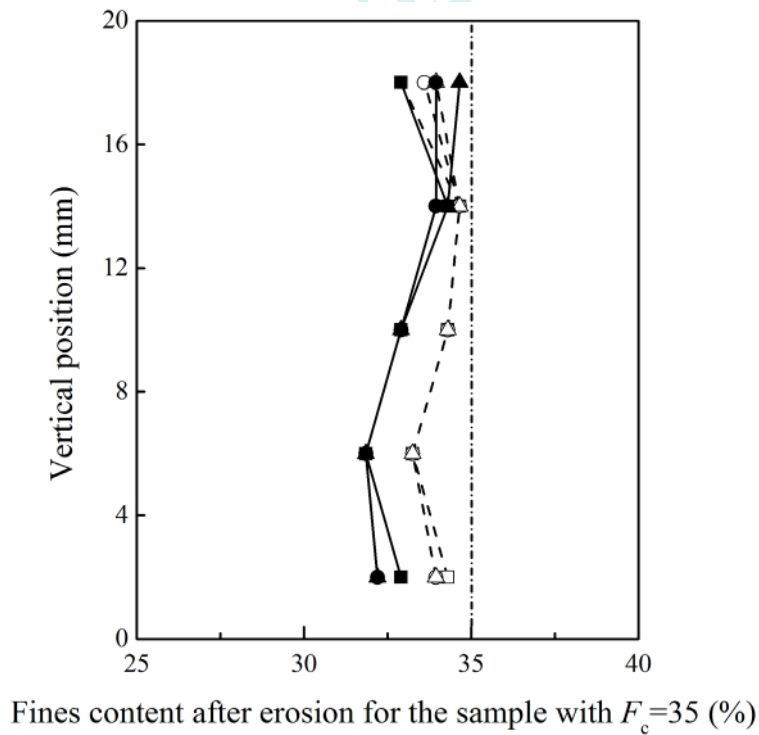


Figure 8 Erosion rate in terms of mass percentage for the samples with (a) $F_c=15\%$ and (b) $F_c=35\%$ under different suspension concentrations (C) and hydraulic gradients (i)



(a)



(b)

Figure 9 Distribution of the fine fraction after erosion along the height of the sample with (a) $F_c=15\%$ (b) $F_c=35\%$

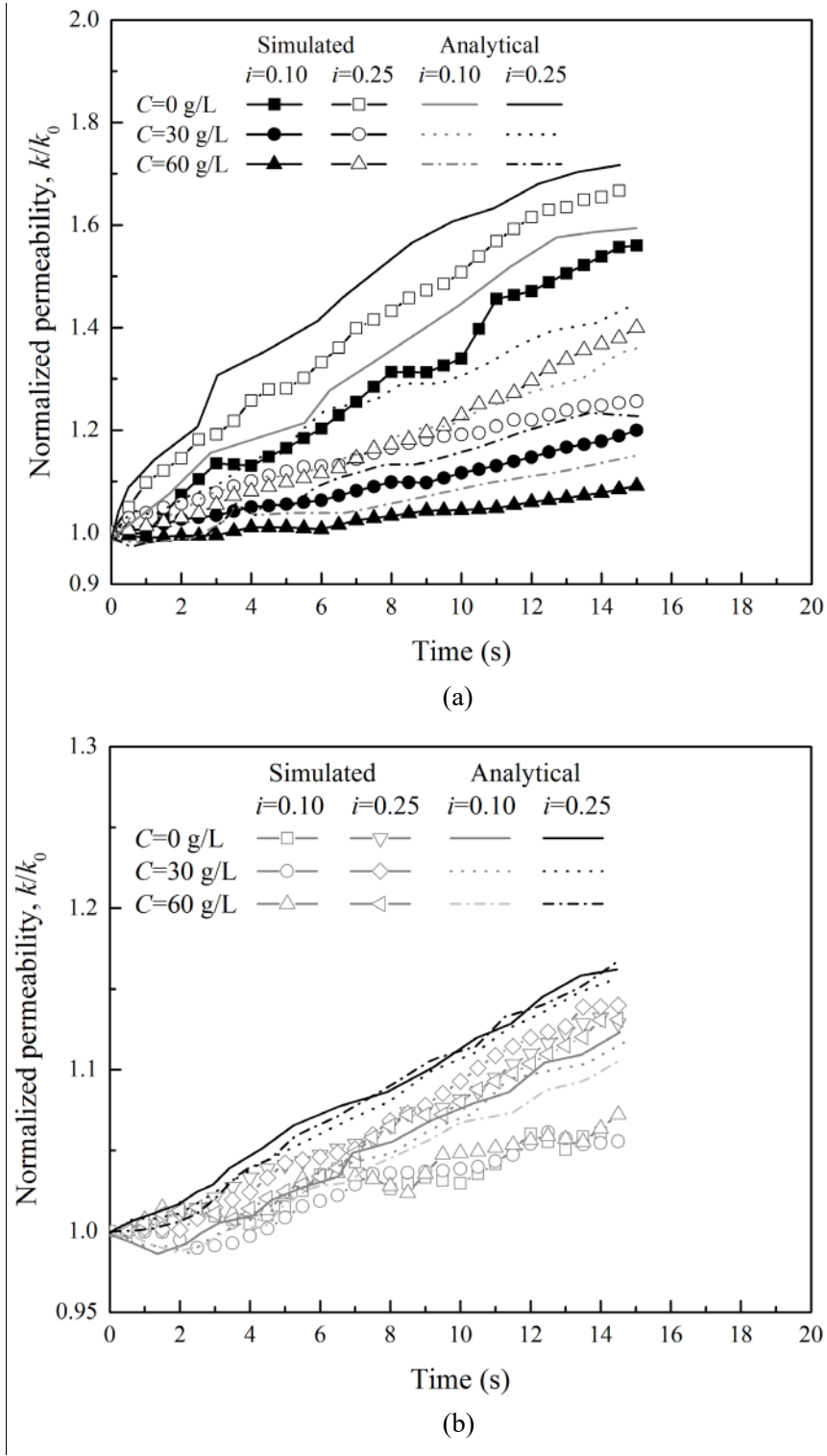


Figure 10 Evolution of the hydraulic conductivity for the sample with (a) $F_c=15\%$ and (b) $F_c=35\%$ (k_0 of the sample with $F_c=15\%$ and 35% are 3.6×10^{-4} cm/s and 1.8×10^{-4} cm/s, respectively)

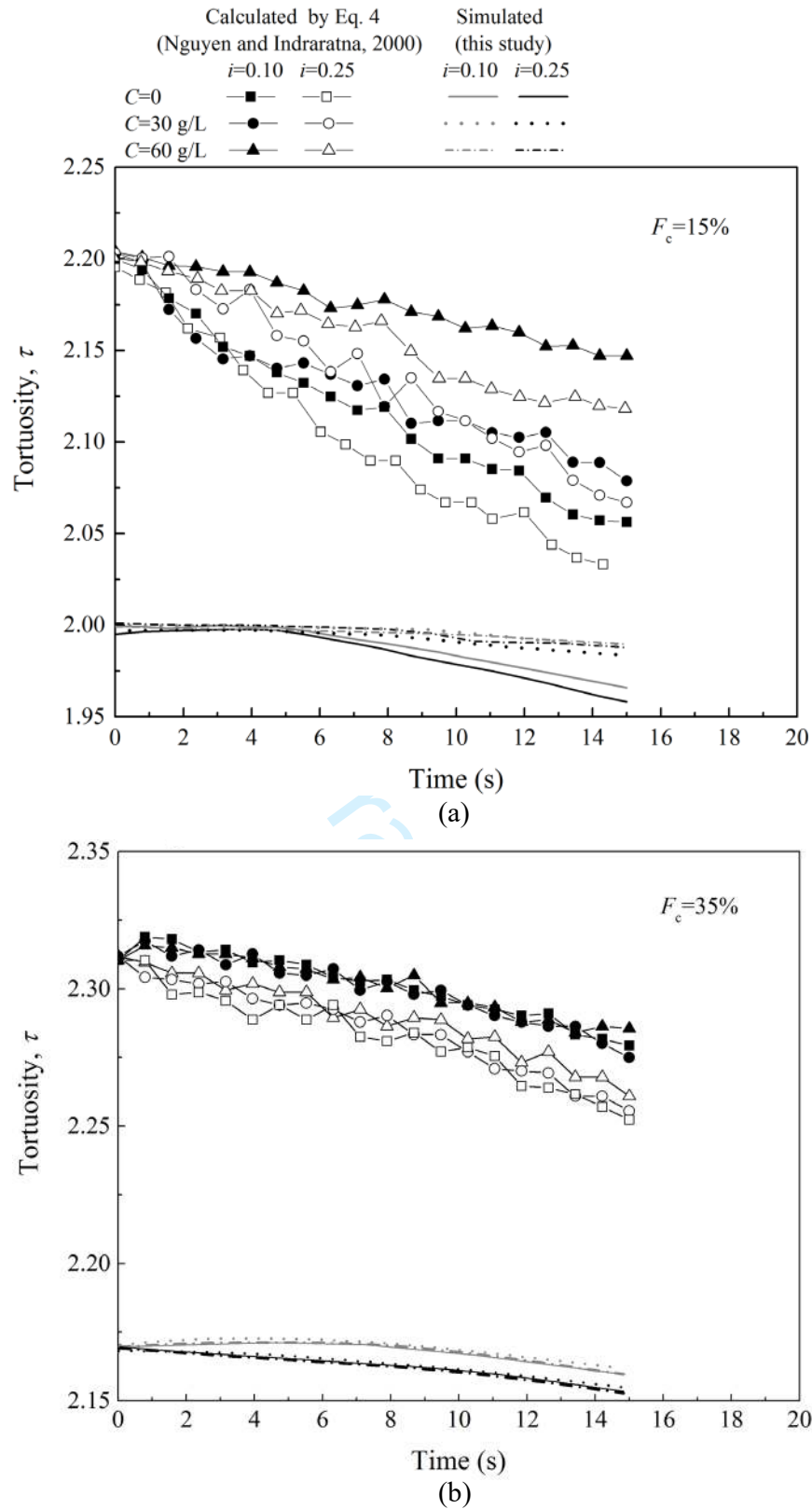


Figure 11 Comparison of the tortuosity (τ) calculated by the approach of this study with that of Nguyen and Indraratna (2020(b)) for the samples with (a) $F_c=15\%$ and (b) $F_c=35\%$

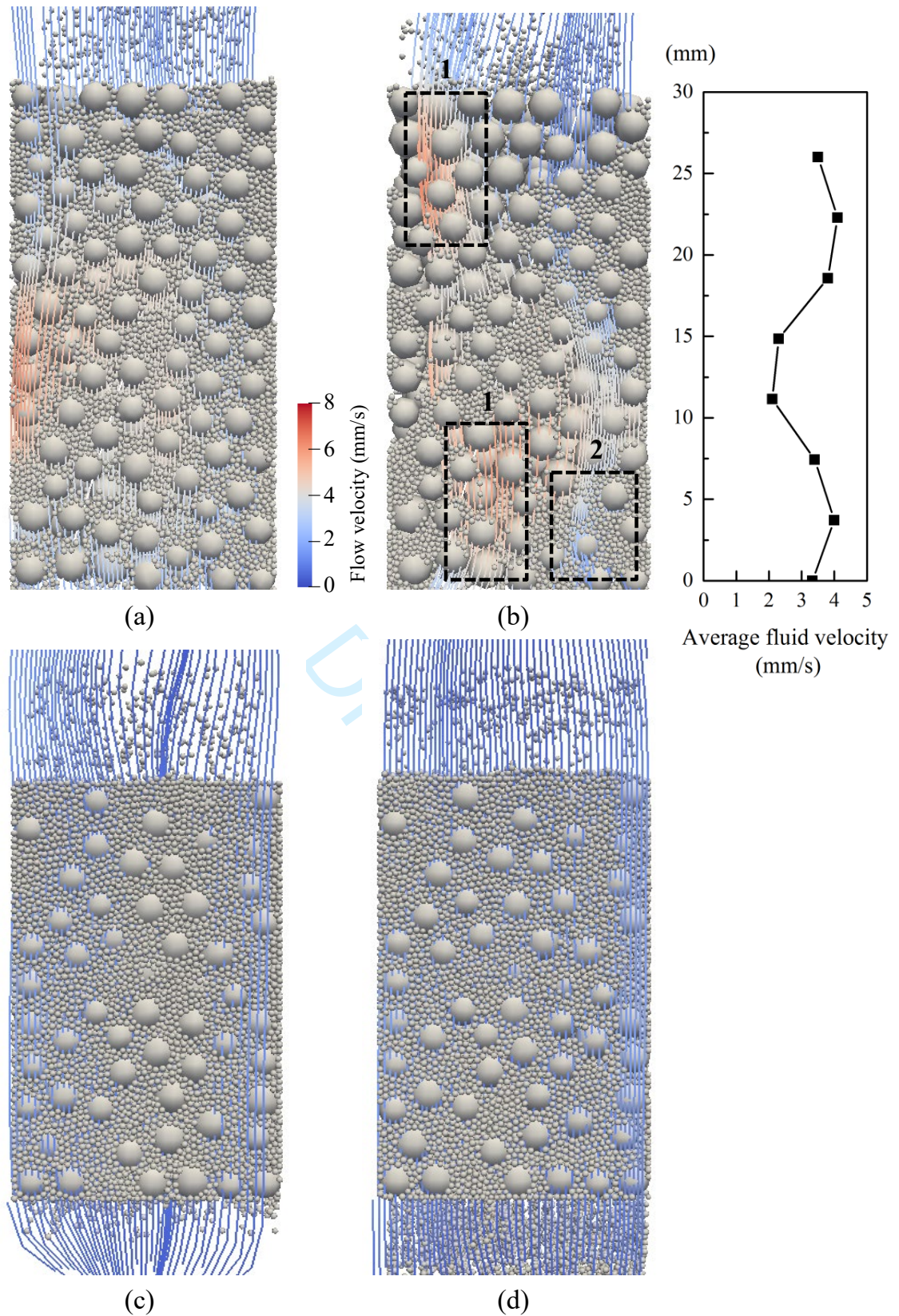


Figure 12 Interaction between fine migration and fluid flow at the (a) initial time and (b) end of the simulation for the sample with $F_c=15\%$ and (c) initial time and (d) end of the simulation for the sample with $F_c=35\%$ under $i=0.25$ and $C=30$ g/L

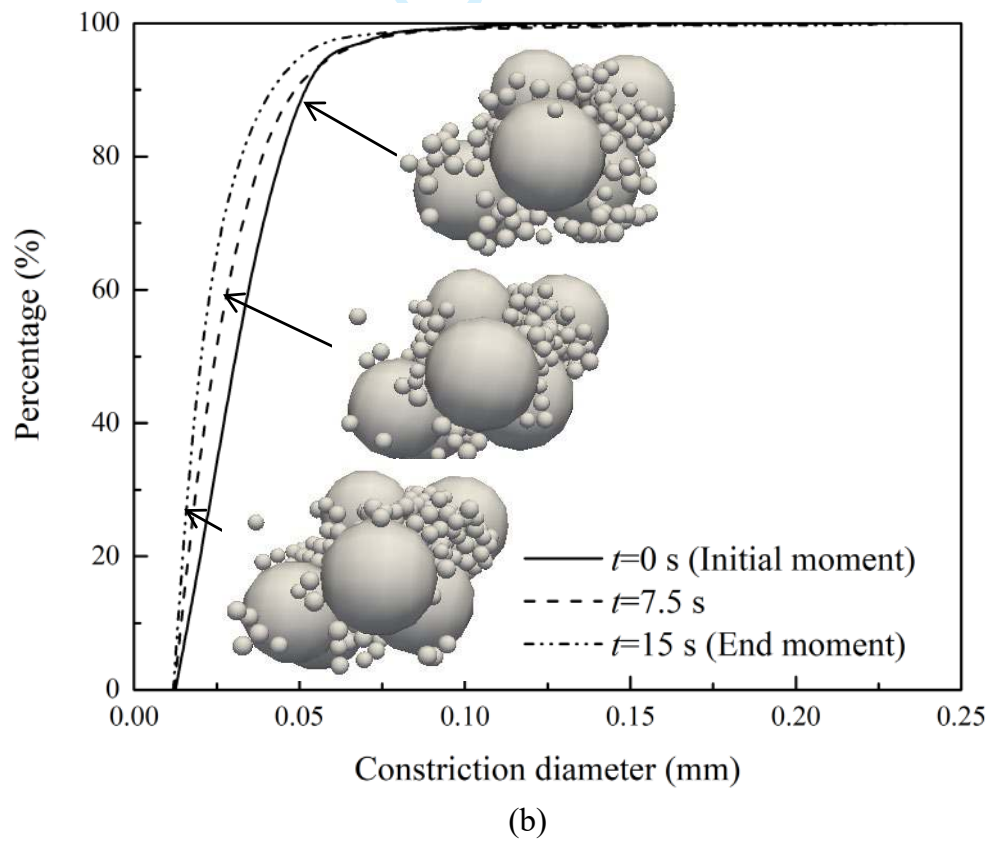
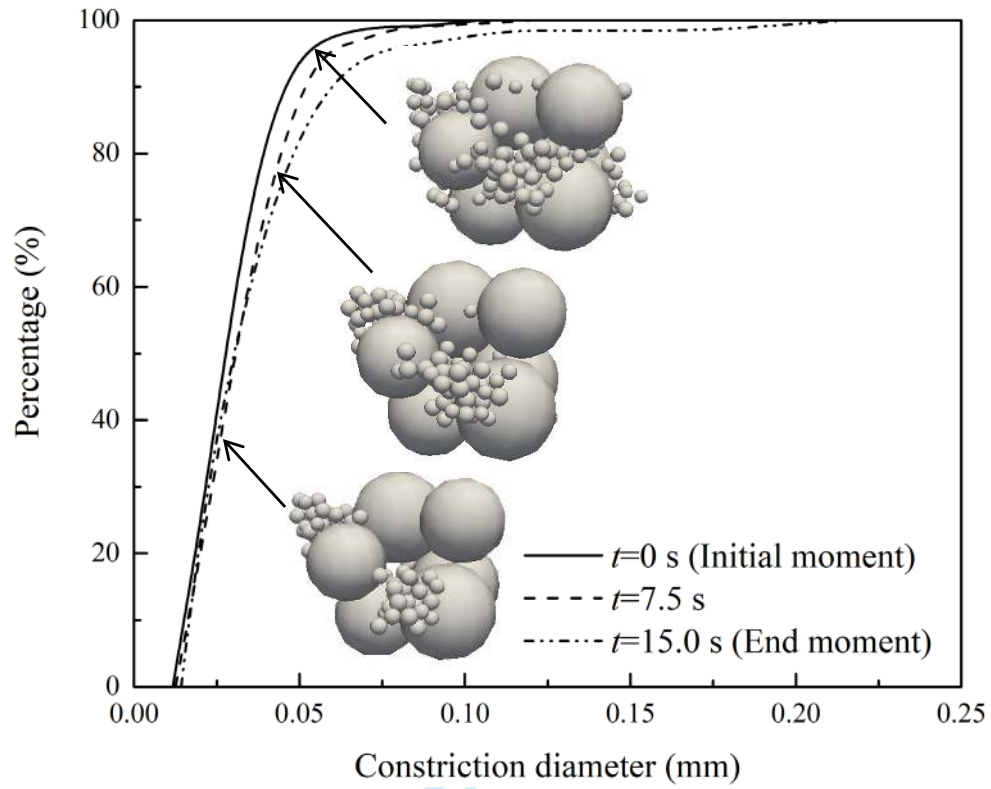


Figure 13 Evolution of the local packing configuration and constriction size distribution for the (a) erosion area and (b) clogging area

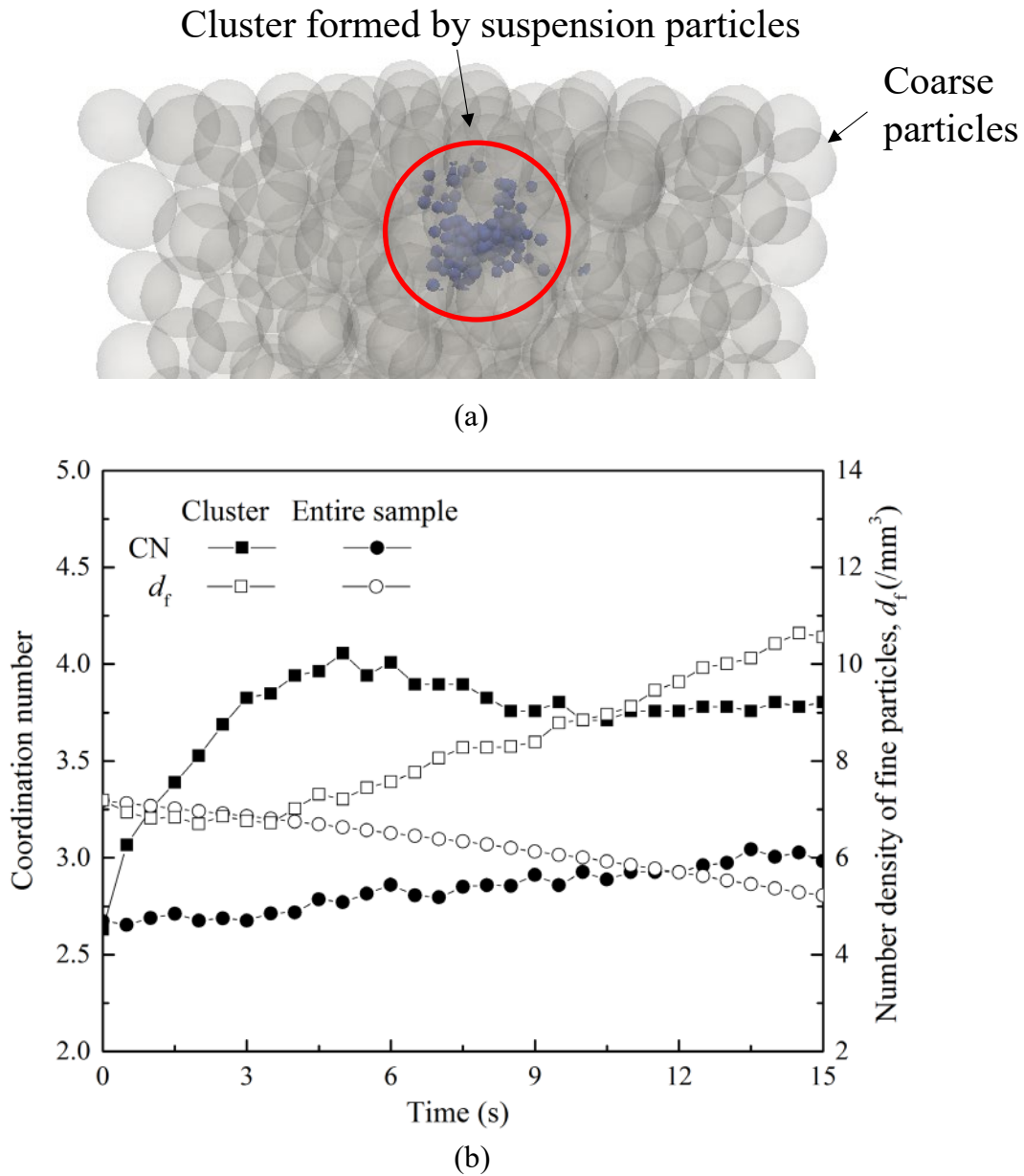
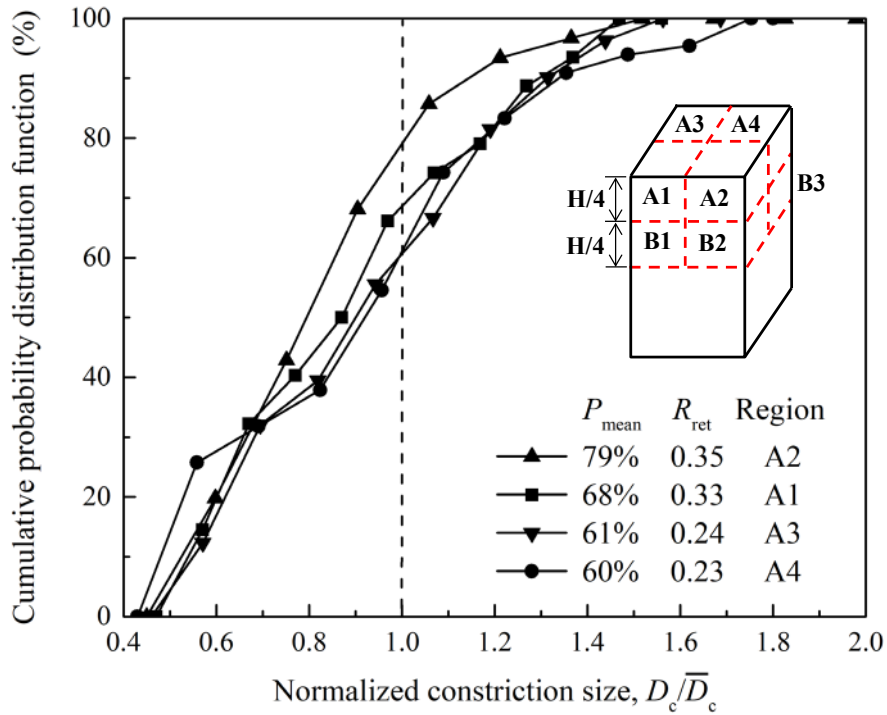
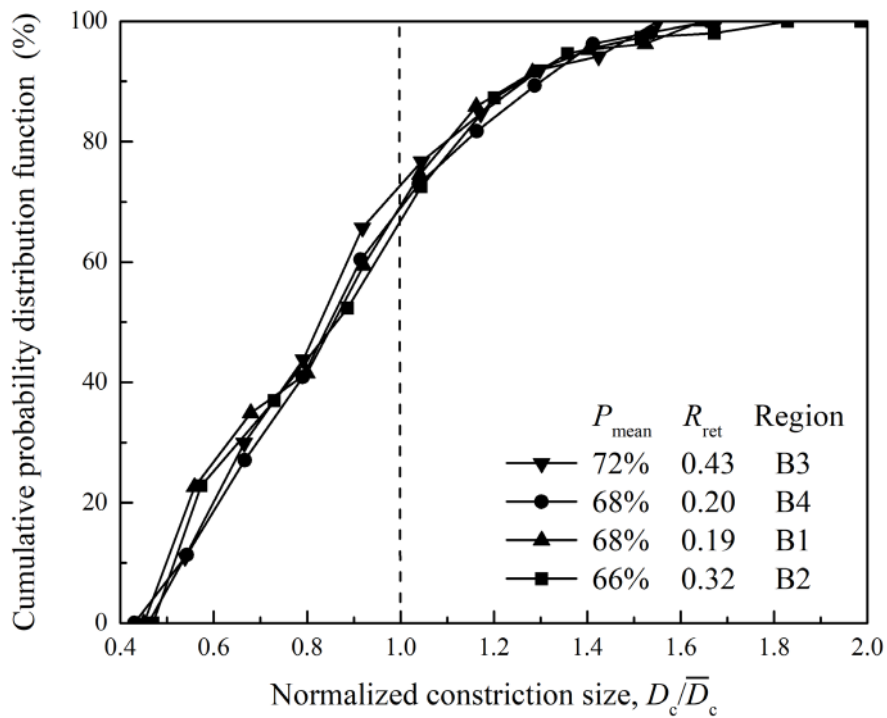


Figure 14 (a) Cluster formed by suspension particles at the top of the sample; (b) coordination number and number density of the fine particles in the cluster and the entire sample



(a)



(b)

Figure 15 Relationship between the constriction size distribution and the retention ratio for (a) region A; (b) region B

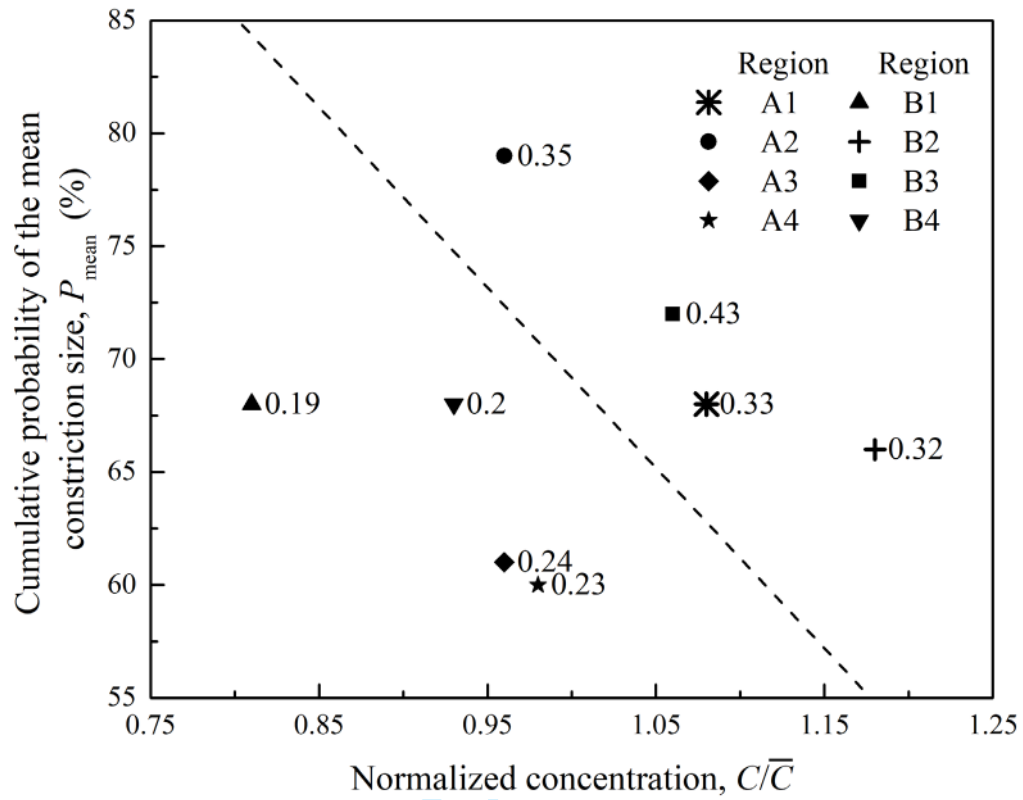


Figure 16 Assessment of the retention ratio based on P_{mean} and concentration (normalized by the average concentration of the eight sub-zones)

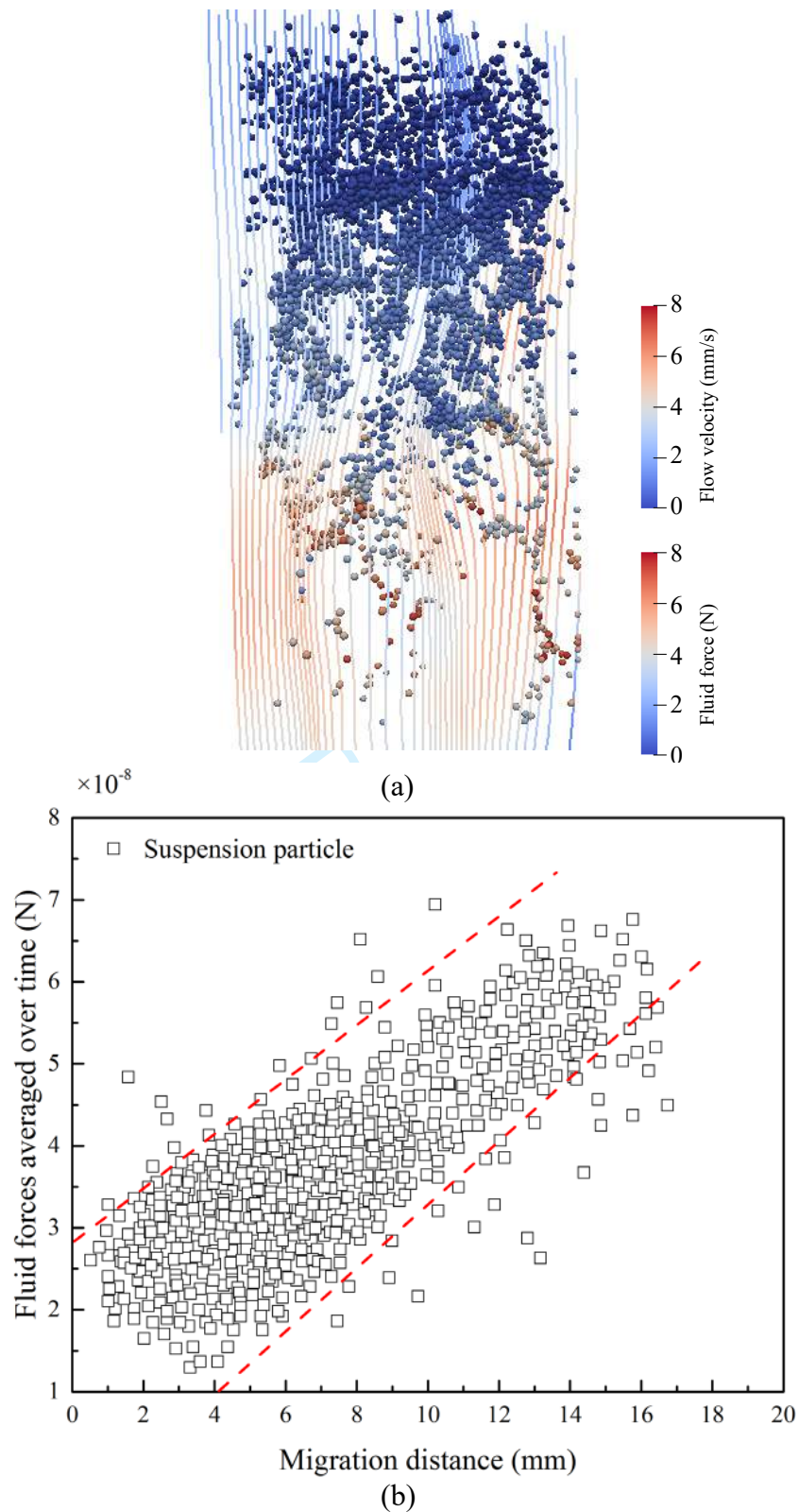


Figure 17 Relationship between the average particle-fluid interaction force during erosion and migration distance for the suspension particles in the case of $F_c=15\%$, $C=70$ g/L, and $i=0.25$ (a) at the end of erosion; (b) during internal erosion

1 Appendix: Coupled CFD-DEM method

2 Governing equations for DEM

3 At any time t , the equation governing the translational and rotational motion of particle i
4 is

$$\begin{cases} m_i \frac{d\mathbf{U}_i}{dt} = \sum_{j=1}^{n_i^c} \mathbf{F}_{ij}^c + \mathbf{F}_i^g + \mathbf{F}_i^f \\ I_i \frac{d\boldsymbol{\omega}_i}{dt} = \sum_{j=1}^{n_i^c} \mathbf{M}_{tij} + \mathbf{M}_{rij} \end{cases} \quad (\text{A1})$$

5 where m_i and I_i denote the mass and moment of inertia of particle i , respectively. \mathbf{U}_i and $\boldsymbol{\omega}_i$
6 are the translational and angular velocities of particle i , respectively. \mathbf{F}_{ij}^c is the contact force
7 acting on particle i by particle j . \mathbf{M}_{tij} and \mathbf{M}_{rij} are the torques acting on particle i by particle
8 j arising from the tangential force and the rolling friction force, respectively. \mathbf{F}_i^f and \mathbf{F}_i^g are
9 the particle-fluid interaction force and gravity force acting on particle i . \mathbf{F}_i^g equals to zero as
10 the gravity force is dismissed in this study.

11 The inter-particle rolling torque is calculated by the directional constant torque model
12 proposed by Zhou et al. (1999):

$$\mathbf{M}_r = -\frac{\boldsymbol{\omega}_i - \boldsymbol{\omega}_j}{|\boldsymbol{\omega}_i - \boldsymbol{\omega}_j|} \mu_r F_n R_r \quad (\text{A2})$$

13 where $\boldsymbol{\omega}_i$ and $\boldsymbol{\omega}_j$ are the angular velocities of two contacting particles i and j , respectively; $|\boldsymbol{\omega}_i -$
14 $\boldsymbol{\omega}_j| = \text{norm of } \boldsymbol{\omega}_i - \boldsymbol{\omega}_j$; μ_r is the coefficient of rolling resistance; and $R_r = \text{rolling radius defined by}$
15 $R_r = r_i r_j / (r_i + r_j)$, where r_i and r_j are radii of contacting particles i and j , respectively. In the DEM
16 code, the Hertzian contact law (Mindlin and Deresiewicz 1953; Renzo and Maio 2004) with
17 Coulomb's friction law is employed to describe the inter-particle contact behavior.

18 **Governing equations for computational fluid dynamics**

19 The CFD code solves the following continuity equation and locally averaged Navier-
20 Stokes equation accounting for the presence of particles in the fluid.

$$\begin{cases} \frac{\partial(n\rho)}{\partial t} + \nabla \cdot (n\rho\mathbf{U}^f) = 0 \\ \frac{\partial(n\rho)}{\partial t} + \nabla \cdot (n\rho\mathbf{U}^f\mathbf{U}^f) - n\nabla \cdot (\mu\nabla\mathbf{U}^f) = -\nabla p - \mathbf{f}^p + n\rho\mathbf{g} \end{cases} \quad (\text{A3})$$

21 where \mathbf{U}^f is the average velocity of a fluid cell. n is the local porosity which is used to
22 account for the particle influence on the fluid computation. p is the fluid pressure, \mathbf{f}^p is the
23 average particle-fluid interaction force per unit volume, ρ and μ is the fluid density and
24 viscosity, respectively. The fluid viscosity is the property of a fluid to be resistant to flow.
25 Fluids with a high viscosity are more resistant to flow. The particle-fluid interaction force (\mathbf{F}_i^f)
26 in Eq (A1) is the fluid force acting on a single particle. The average particle-fluid interaction
27 force (\mathbf{f}^p) in Eq (A3) is the reaction force of the \mathbf{F}_i^f within the volume of a fluid cell. As
28 gravity is not considered in this study, the gravitational component in this equation equals to
29 zero.

30 **Governing equations for particle-fluid interaction forces**

31 In this study, the particle-fluid interaction forces, including the drag force (\mathbf{F}^d), pressure
32 gradient force (\mathbf{F}^p) and viscous force (\mathbf{F}^v), are considered as shown in Eq. A4 (Hu et al. 2018).

$$\mathbf{F}^f = \mathbf{F}^d + \mathbf{F}^p + \mathbf{F}^v \quad (\text{A4})$$

33 The drag force is adopted from the expression proposed by Di Felice (1994), which is
34 applicable for a dense granular regime and valid for a wide range of Reynolds numbers:

$$\left\{ \begin{array}{l} \mathbf{F}^d = \frac{1}{8} C_d \rho \pi d_p^2 (\mathbf{U}^f - \mathbf{U}^p) |\mathbf{U}^f - \mathbf{U}^p| n^{1-\chi} \\ C_d = \left(0.63 + \frac{4.8}{\sqrt{\text{Re}_p}} \right)^2 \\ \text{Re}_p = \frac{n \rho d_p |\mathbf{U}^f - \mathbf{U}^p|}{\mu} \\ \chi = 3.7 - 0.65 \exp\left[-\frac{(1.5 - \log_{10} \text{Re}_p)^2}{2}\right] \end{array} \right. \quad (\text{A5})$$

35 where d_p is the diameter of particles and C_d is the particle-fluid drag coefficient for a single
 36 spherical particle that depends on the Reynolds number of the particle (Re_p). χ in Eq. A5 is a
 37 correlation function that modifies the coefficient of drag force accounting for the presence of
 38 other particles in the system.

39 The pressure gradient force (\mathbf{F}^p) and viscous force for a single particle are formulated by
 40 Eqs. (A6) and (A7), respectively (Zhou et al. 2010):

$$\mathbf{F}^p = -V_p \nabla p \quad (\text{A6})$$

$$\mathbf{F}^v = -V_p \nabla \cdot \boldsymbol{\tau} \quad (\text{A7})$$

41 where $\boldsymbol{\tau}$ is the viscous stress tensor which describes the friction between the fluid and the
 42 surface of particles.